(2)

GL-TR-90-0171

Physical Property Measurements on Analog Granites Related to the Joint Verification Experiment

Randolph J. Martin, III
Karl B. Coyner
Robert W. Haupt

New England Research, Inc
76 Olcott Drive
White River Junction, VT 05001

August 15, 1990

Scientific Report No. 1

GEOPHYSICS LABORATORY
AIR FORCE SYSTEMS COMMAND
UNITED STATES AIR FORCE
HANSCOM AIR FORCE BASE, MASSACHUSETTS 01731-5000

SPONSORED BY
Defense Advanced Research Projects Agency
Nuclear Monitoring Research Office
ARPA ORDER NO 5307

MONITORED BY
Geophysics Laboratory
F19628-89-C-0097

The views and conclusions contained in this document are those of the authors and should not be interpreted as representing the official policies, either expressed or implied, of the Defense Advanced Research Projects Agency or the U.S. Government.

This technical report has been reviewed and is approved for publication.

JAMES F. LEWKOWICZ
Contract Manager
Solid Earth Geophysics Branch
Earth Sciences Division

JAMES F. LEWKOWICZ
Branch Chief
Solid Earth Geophysics Branch
Earth Sciences Division

FOR THE COMMANDER

DONALD H. ECKHARDT, Director
Earth Sciences Division

This report has been reviewed by the ESD Public Affairs Office (PA) and is releasable to the National Technical Information Service (NTIS).

Qualified requestors may obtain additional copies from the Defense Technical Information Center. All others should apply to the National Technical Information Service.

If your address has changed, or if you wish to be removed from the mailing list, or if the addressee is no longer employed by your organization, please notify GL/IMA, Hanscom AFB, MA 01731-5000. This will assist us in maintaining a current mailing list.

Do not return copies of this report unless contractual obligations or notices on a specific document requires that it be returned.

UNCLASSIFIED
SECURITY CLASSIFICATION OF THIS PAGE

REPORT DOCUMENTATION PAGE

Form Approved OMB No. 0704-0188

1a. REPORT SECURITY CLASSIFICATION UNCLASSIFIED	1b. RESTRICTIVE MARKINGS
2a. SECURITY CLASSIFICATION AUTHORITY	3. DISTRIBUTION/AVAILABILITY OF REPORT Approved for Public Release, Distribution Unlimited
2b. DECLASSIFICATION/DOWNGRADING SCHEDULE	
4. PERFORMING ORGANIZATION REPORT NUMBER(S)	5. MONITORING ORGANIZATION REPORT NUMBER(S) GL-TR-90-0171
6a. NAME OF PERFORMING ORGANIZATION New England Research, Inc.	6b. OFFICE SYMBOL (If applicable)
6c. ADDRESS (City, State, and ZIP Code) 76 Olcott Drive White River Jct. VT 05001	7a. NAME OF MONITORING ORGANIZATION Geophysics Laboratory
8a. NAME OF FUNDING/SPONSORING ORGANIZATION DARPA	8b. OFFICE SYMBOL (If applicable) NA
8c. ADDRESS (City, State, and ZIP Code) 1400 Wilson Boulevard Arlington, VA 22209	7b. ADDRESS (City, State, and ZIP Code) Hanscom AFB, MA 01731-5000
	9. PROCUREMENT INSTRUMENT IDENTIFICATION NUMBER F19628-89-C-0097
	10. SOURCE OF FUNDING NUMBERS

PROGRAM ELEMENT NO.	PROJECT NO.	TASK NO.	WORK UNIT ACCESSION NO.
62714E	9A10	DA	BD

11. TITLE (Include Security Classification) (U)
Physical Property Measurements on Analog Granites Related to the Joint Verification Experiment

12. PERSONAL AUTHOR(S)
Randolph J. Martin, III, Karl B. Coyner, Robert W. Haupt

13a. TYPE OF REPORT	13b. TIME COVERED	14. DATE OF REPORT (Year, Month, Day)	15. PAGE COUNT
Scientific Report 1	FROM 5/15/89 TO 5/14/90	8/15/90	96

16. SUPPLEMENTARY NOTATION
USSR)

17. COSATI CODES			18. SUBJECT TERMS (Continue on reverse if necessary and identify by block number)
FIELD	GROUP	SUB-GROUP	attenuation, JVE rock properties

19. ABSTRACT (Continue on reverse if necessary and identify by block number)

A key element in the ~~Joint Verification Experiment~~ JVE conducted jointly between the United States and the ~~Soviet Union~~ is the analysis of the geology and physical properties of the rocks in the respective test sites. A study ~~has been~~ was initiated to examine unclassified crystalline rock specimens obtained from areas near the Soviet site, Semipalatinsk and appropriate analog samples selected from Mt. Katadin, Maine. These rocks were also compared to Sierra White and Westerly Granite which have been studied in great detail. ~~The following measurements were performed~~ were to characterize these rocks:

(1) Uniaxial strain with simultaneous compressional and shear wave velocities;
(2) Hydrostatic compression to 150 MPa with simultaneous compressional and shear wave velocities;
(3) Attenuation measurements as a function of frequency and strain amplitude for both dry and water saturated conditions.

20. DISTRIBUTION/AVAILABILITY OF ABSTRACT	21. ABSTRACT SECURITY CLASSIFICATION
☒ UNCLASSIFIED/UNLIMITED ☐ SAME AS RPT. ☐ DTIC USERS	UNCLASSIFIED

22a NAME OF RESPONSIBLE INDIVIDUAL	22b TELEPHONE (Include Area Code)	22c OFFICE SYMBOL
James F. Lewkowicz	617-377-3222	LWH

DD Form 1473

UNCLASSIFIED

The elastic moduli determined from the hydrostatic compression and uniaxial strain test show that the rock matrix/mineral properties for the above mentioned rocks are comparable in magnitudes which vary within 25% from sample to sample. These properties appear to be approximately isotropic, especially at high pressures. However, a degree of anisotropy is evident for certain samples at pressures below 35 MPa and is attributed to dominant pre-existing microcrack populations and their alignments. The largest moduli changes are observed while loading up to 35 MPa. At this low pressure range the static moduli typically increased 100% while the increase in the dynamic moduli was only as much as 30%. Within the range of error, the static moduli did not exceed the dynamic moduli. At pressures and mean stresses above 35 MPa, the crack populations have been significantly closed, the degree of anisotropy is greatly diminished to within 10%, and the static and dynamic moduli merge in value differing within 15%.

The dependence of extensional attenuation ($Q^{-1}E$) and Young's modulus (E) on strain amplitude were experimentally determined for intact Sierra White granite at strain amplitudes between 10^{-7} and 10^{-3} using the hysteresis loop technique. Measurements were conducted at a frequency of 0.1 Hz on both a room dry and water-saturated sample, and at several levels of elevated axial load to 20 MPa. The experimental data indicate that the dependence of attenuation of strain amplitude follows a sigmoidal shaped curve with at least three distinct regions of behavior. Attenuation is linear, or independent of strain amplitude, at strain amplitudes less than approximately 10^{-5}, with a $Q^{-1}E$ of roughly 0.008 at room dry conditions. At strain amplitudes greater than 10^{-5} attenuation becomes nonlinear, or dependent on strain amplitude, and increases dramatically to a $Q^{-1}E$ of about 0.05 at 10^{-4} strain. There is a linear dependence on strain amplitude. A frictional attenuation mechanism across crack surfaces and at point contacts is suggested by the strain amplitude dependent behavior. Maximum attenuation was attained at 10^{-4} strain; at higher strains attenuation levelled off or decreased slightly. This is an upper bound on frictional attenuation, limited by crack closure or maximum motion across sliding surfaces. For the water-saturated sample, attenuations are larger by approximately a factor of 2, and the same general trends were observed.

Keywords: Rock mechanics; Granite cracks attenuation; Joint test evaluation. (EDB)

TABLE OF CONTENTS

SECTION 1

Physical Property Measurements on Analog Granites Related to the Joint Verification Experiment

Randolph J. Martin and Robert W. Haupt
New England Research, Inc.
White River Junction, Vermont

INTRODUCTION

A Joint Verification Experiment (JVE) was performed as part of the test ban treaty protocol between the United States and the Soviet Union. This program consisted of an exchange of data and rock cores for a nuclear test at the Soviet test site near Shagan River and a nuclear explosion at the Nevada Test Site. Scientists from both countries, not only observed each shot, but fielded instrumentation to directly measure the yield and and near field source characteristics. In order to quantify the near and far field effects observed at Semipalatinsk, the physical properties of the rocks near ground zero must be determined for use in existing models. The rocks supplied by the Soviet Union are confidential and the measurements of the physical rock properties are classified. Consequently, a program is underway to completely characterize a suite of hard, brittle rocks similar in composition and geologic history to those present at the Soviet test site.

Understanding and modelling seismic wave propagation from nuclear explosions requires information on the behavior of rocks in the source region under appropriate loading conditions. Within the source region, the rocks are loaded in uniaxial strain; during unloading damage occurs permanently altering the rocks. Outside the source region, strains are below 10^{-6} in which deformation is elastic. In order to characterize rock behavior under such a wide range of conditions several approaches have been pursued. Laboratory measurements of rock properties under static and dynamic conditions have been

conducted in uniaxial strain, uniaxial stress, and hydrostatic compression; simultaneous compressional and shear wave velocity measurements accompanied each experiment. These data are used to calculate static and dynamic elastic moduli and attenuation as function of mean stress and strain amplitude. The computed coefficients can then be incorporated into forward models to determine: particle velocity and displacements, and time histories in the nearfield (Stevens, et. al, 1986). The predicted results are then compared with scale model experiments performed on hard brittle rocks using small explosive charges (Nagy and Florence, 1987; Miller and Florence, 1990). The analysis of analog granite samples collected near Mt. Katahdin, ME is underway at Lamont-Doherty Geological Observatory, SRI, and New England Research.

EXPERIMENTAL PROCEDURE

The elastic properties of a suite of rock cores were determined from hydrostatic and uniaxial strain experiments with simultaneous ultrasonic velocity mea urements. These rocks included (1) three specimens from the region near Semipalatinsk, USSR, (2) a fine and coarse grained granite from Mt. Katahdin, ME (3) and two well characterized granites, Westerly and Sierra White.

The compositions, densities, and grain diameters were measured and analyzed for each rock. The mineral compositions compare closely. The major mineral constituents for each rock were 40-50% microcline, 10-40% quartz, 2-40% albite. Dry bulk densities range 2.577-2.688 g/cm^3; the porosity for each rock was approximately 1%. The mean grain diameters ranged between 0.40 and 1.04 mm. The modal analysis and mean grain diameter for each rock are given in Table 1. Photomicrographs are presented for all the specimens in Plates C-1 through C-7 in Appendix C.

Several hand specimens from the vicinity of the Soviet test site at Shagan river near Semipalatinsk were studied. These specimens were not related to the protocol for the Joint Verification Experiment (JVE); consequently, the results are not classified. One specimen was a granite recovered at a depth of 34 meters from a NRDC borehole south of Semipalatinsk. Two other samples, an altered quartz diorite and a monzonite, were collected from the surface located at the northwest corner of the test site. The quartz diorite is heavily altered and strongly sheared. The monzonite specimen showed pronounced slickensides on two surfaces. The granite was relatively unaltered and did not exhibit significant fractures, at least in the core reported on in this study.

The USGS has identified a granite near Mt. Katahdin, ME as a possible analog to the rocks near Semipalatinsk. In particular, these Katahdin granites have similar compositions, grain sizes, and geological histories to those near Semipalatinsk. The two rocks, a fine and coarse grained granite, are being characterized by scientists at Lamont-Doherty Geological Observatory and New England Research, Inc. (NER). NER is (1) determining the relationship between static and dynamic elastic moduli and (2) measuring seismic wave attenuation (Q^{-1}) as a function of frequency and strain amplitude. In addition Westerly granite, from Westerly, RI and Sierra White granite from Raymond, CA have been

included for completeness. Both of these granites have been well documented in the literature. Furthermore, scale model experiments have been carried out on Sierra White granite by Nagy and Florence (1986). Berea sandstone from Berea, OH was also studied and compared to the granites. The main reason for including a sandstone is that it has a markedly different pore structure from the crystalline rocks.

Sample Preparation

Each test specimen was a ground right circular cylinder 2.54 cm in diameter and between 3.4 cm to 5.0 cm in length. After each specimen was dimensioned and weighed it was jacketed with 0.13 mm thick copper to prevent the confining medium from penetrating into the sample. The jacket was approximately 0.25 cm longer at each end of the sample to provide for sealing the jacketed sample to the ultrasonic transducers positioned at each end of the specimen. Prior to instrumenting the sample with strain gages, the jacket was seated to the specimen at a confining pressure of 14 MPa; then the copper jacket was sanded and cleaned with acetone. A minimum of two strain gages, Micro-Measurements CEA-06 250UW-120, were epoxied to the copper jacket. One gage was positioned on the cylindrical surface with its grid aligned parallel to the sample axis (axial); the other was oriented normal to the axis (radial). In some instances three radial gages were positioned around the specimen.

Each ultrasonic transducer contained the compressional and shear crystals mounted on titanium end pieces and isolated from the confining medium. The sample core was placed between the two titanium end pieces. Gum rubber tubing was clamped over the sample/titanium interface to seal the joint. Electrical leads were soldered to the gages and were connected to high-pressure electrical ports on the lower ultrasonic transducer. The sample assembly was then inserted into a 200 MPa pressure vessel with a 5.5 cm diameter bore. The pressure vessel was mounted in a servo-controlled loading frame.

Experimental Apparatus

The servo-controlled loading frame exerted an axial load on the sample column. The servo-controller is a self-contained digital unit, which operates in either force or

displacement feedback. The unit generates a reference signal for the servo-amplifier, in one of three possible modes: (i) ramp to upper limit at constant rate and hold, (ii) ramp to lower limit at a constant rate and hold, and (iii) saw-tooth between upper and lower limits at a constant rate. The upper and lower limits and the rate are manually set. The rate at which the reference signal is updated can be varied from 10^3 to 10^{-5} times per second. The loading rate or displacement rate of the hydraulic press depends on the range of the feedback transducers. The feedback transducers are conditioned with amplifiers in the servo-control unit and balanced so that the full scale output of the transducer corresponds to the maximum range of the reference signal generator. The full scale output (10 volts) is divided into 2^{12} discrete steps. The rate is controlled by varying the time between steps. For these experiments the press was operated in displacement feedback; the force was measured with an external load cell

The confining pressure was generated and maintained with a servo-controlled pressure intensifier. The pressure output was measured with a Sensotec model Z/108-04 pressure transducer. Either the pressure transducer or the radial strain gage was used as the feedback signal for the confining pressure system. Hydraulic oil was used as a confining medium. All data was recorded using an IBM/PC based data acquisition system. The data acquisition program, ACQUIRE, developed at NER was used to collect and store the data. The schematic of the experimental configuration is shown in Figure 1.

Ultrasonic Velocity Measurement

The compressional (P) and shear (S) wave velocities for the rock, at any stress condition, were obtained by measuring the one way travel time of a P or S wave through the core and dividing by the sample length. The wave propagation direction was parallel to the core axis. The ultrasonic transducer consisted of a piezoelectric source and receiver pair of like crystals (P or S) positioned at opposing ends of the cylindrical core. Only one crystal pair could be activated at a time. The source crystal was driven with a short electrical pulse (center frequency of 1 MHz) generated with a Panametrics 5055PR pulser-receiver.

The signal from the receiver crystal was amplified, high-pass filtered at 0.3 MHz, and

displayed on a LeCroy 9400 digital oscilloscope. The travel time was measured on the oscilloscope screen with a cursor control marking the first break of the signal. The break was defined by a threshold voltage that was 1.25% of the peak-to-peak amplitude of the first three half-cycles of the signal. The arrival time was picked at the point when the threshold voltage was exceeded relative to the baseline voltage and had a resolution of ± 0.01 microsecond. The travel time of the wave through the end pieces is subtracted form the total time measured on the oscilloscope. The travel times of P and S wave propagation through the titanium end pieces or *zero times* were measured as a function of confining pressure by placing the end pieces head to head.

Hydrostatic compression with compressional and shear wave velocities

In order to characterize the physical rock properties of the samples, two separate experiments were performed on each sample (1) hydrostatic compression with compressional and shear wave velocities and (2) uniaxial strain with compressional and shear wave velocities.

Anisotropy is prevalent in crystalline rocks, especially at low confining pressures. In order to define the magnitude of the anisotropy and its pressure dependence, the strain developed during hydrostatic compression were measured as a function of orientation with respect to the core axis. Using these data, the principal strain directions were determined and the degree of anisotropy established.

Four strain gages were epoxied to the copper jacket; one axial and three radial. The set of three radial gages, spaced 120° apart, were referenced to an arbitrary point, P, on the core circumference. The positions of the strain gages relative to the rock core and principal directions are shown in Figure 2. The data acquired in these directions can be used to determine the strains in the principal directions at any confining pressure. The technique for determining strains in the principal directions is discussed in detail by Scholz and Kcozynski [1979]. The radial strains ε_P, ε_Q, ε_R can be used to compute the principal strains in the radial directions, ε_2 and ε_3, and the angle, θ formed between ε_P and ε_2. ε_1 is chosen to be in the axial direction. Points Q and R are 120 degrees apart from point, P.

The solutions for strain are shown below (Jaeger, 1962) :

$$\varepsilon_2 + \varepsilon_3 = \varepsilon_P + \varepsilon_R \qquad (1)$$

$$\varepsilon_2 - \varepsilon_3 = [(\varepsilon_P - 2\varepsilon_Q + \varepsilon_R)^2 + (\varepsilon_{\cdot} - \varepsilon_R)^2]^{1/2} \qquad (2)$$

$$\tan 2\theta = (\varepsilon_P - 2\varepsilon_Q + \varepsilon_{\cdot})/(\varepsilon_P - \varepsilon_R) \qquad (3)$$

In particular, the differences in the strains in the principal directions as a function of pressure are used to determine the degree of anistropy in the rock properties and crack population alignments of each sample.

Each rock was tested by incrementally increasing the confining pressure to 150 MPa and then downloading. Ultrasonic compressional (P) and shear (S) wave velocities were measured at pressures of 5, 10, 20, 40, 75, 100, 125 MPa for the hydrostatic loading as well as unloading.

Once the measurements were completed, the elastic moduli were computed. The static bulk modulus, K_s, and linear compressibilities in the principal directions, β_i were calculated from the pressure vs strain data; the dynamic bulk modulus, K_d, was computed from the compressional and shear wave velocities, V_p and V_s, respectively. The volumetric strain data, K_s, K_d, β_i, V_p and V_s for each rock specimen as a function of pressure are shown graphically in Appendix A. A polynomial fit is applied to the raw pressure and strain data sets to remove high frequency and low amplitude noise form the acquired signals. The linear compressibilities and static bulk modulus are then computed from the fitted pressure and strain data. Values of β_i, K_s, K_d, V_p and V_s for selected confining pressures are summarized in Table 2.

Uniaxial Strain with Ultrasonic Velocities

Since uniaxial strain conditions prevail during explosive loading, it is necessary to characterize the rocks for this loading condition and to compare the results with those obtained during hydrostatic loading. In these experiments, the specimen was monotonically loaded at a constant rate while holding the lateral (radial) strain constant. Consequently, the confining pressure increases throughout the loading cycle and decreases during unloading. Ultrasonic P and S wave velocities were measured at confining pressures of 5, 10, 20, 40, 75, 100, 125, and 150 MPa.

The elastic moduli were computed from the experimental data. The static shear, bulk, and Young's moduli and Poisson's ratio (G_s, K_s, E_s, and ν_s) were computed form the stress vs. strain and pressure vs. strain data. The dynamic shear, bulk, and Young's moduli and Poisson's ratio, G_d, k_d, E_d, and ν_d are computed from the ultrasonic velocity data. The axial strain data, the compressional and shear wave velocity data, and the static and dynamic moduli as a function of mean stress for each rock specimen are shown graphically in Appendix B. Values of the static and dynamic moduli and V_p and V_s are presented in Table 3.

EXPERIMENTAL RESULTS

The elastic coefficients computed from the hydrostatic compression and uniaxial strain experiments for the three Soviet and Katahdin specimens agree favorably with those of Westerly and Sierra White granites. The largest differences occur at pressures lower than 35 MPa. These results were also compared to those of the Berea sandstone sample for completeness. The crystalline samples are considerably stiffer than the sandstone and exhibit smaller strains with increasing load. Moreover, since the sandstone is more compliant than the other samples, the crystalline rock moduli and seismic wave velocities are consistently larger than those of the sandstone. Comparisons of the Soviet , Katahdin granites, Westerly granite, Sierra White granite and Berea sandstone are presented in Tables 2 and 3. The complete data for all the experiments are graphically presented in Appendices A and B and are discussed in detail next.

Hydrostatic Compression Tests

It appears that the crack populations and distributions are significant factors in the observed strains as a function of pressure. Moreover, these strains were used to define the rock properties and their orientations. Linear compressibility data were computed from the changes in strain in a given directions as a function of pressure change. For all experiments, the 1 direction is parallel to the core axis while the 2 and 3 directions are in radial lines. Principal directions 1, 2, and 3 form an orthogonal set and are shown relative to the sample core in Figure 2.

For simple hydrostatic compression the linear compressibility in a principal direction, β_i is defined as the ratio of the change in strain in that direction per pressure increment:

$$\beta_i = \frac{\Delta \varepsilon_i}{\Delta P} \qquad (4)$$

where $\Delta\varepsilon_i$ is the strain change in the principal direction and ΔP is the pressure change. The

Katahdin fine grained granite sample exhibits a distinct linear compressibility anisotropy below 50 MPa (see Appendix A, Figure A-5). The compressibility in the 1 direction, β_1 is more than one and one half times larger than β_2 and β_3 at very low pressures, less than 5 MPa. As the confining pressure is increased to 50 MPa, the degree of anisotropy greatly diminishes. Above 50 MPa β_1 , β_2 , and β_3 converge to a single value indicating that the sample exhibits isotropic characteristics at higher pressures.

The linear compressibility data suggest that several of the samples are anisotropic at low pressures and isotropic at high pressures. In particular, crack populations have a certain alignment within each sample. At low pressures, the cracks begin to close with increasing pressure. The change in strain exhibits two distinct characteristics. First, changes in the slope of the linear compressibility at low pressures indicate the closure of elliptically and penny shaped cracks. The ellipticity of a crack can be quantified by its aspect ratio which is the ratio of crack width and length; for further detail see Walsh [1965], O'Connell and Budiansky [1974], and Simmons, et al. [1974]. Second, differences in the linear compressibilities in the principal directions at a given pressure are dependent on the crack alignment. In particular, crack populations may have preferred alignments within the rock and are indicative of the thermal and stress history. At lower pressures, the cracks begin to close and the strains at a given pressure will vary with crack alignment. The strains normal to the plane of the crack are larger than the strains parallel to the long axis of the crack. Both the slope of the linear compressibility and the strain variation with orientation are indicative of the crack aspect ratio. As the aspect ratio approaches unity:

(1) the crack becomes spherical in shape,
(2) the slope of the linear compressibility in the principal directions approach a constant value, and
(3) the variation in strain for a given pressure change as a function of angle with crack population alignment approaches zero.

Major slope changes in the linear compressibilities in the principal directions are observed for all the rocks at pressures up to 35 MPa. Above 35 MPa the slopes approach a constant value. The data suggests that populations of elliptically and penny shaped cracks

are closing with hydrostatic loading up to 35 MPa. In Westerly granite for example (see Appendix A, Figure A-6), the sets of crack populations are randomly aligned with the principal directions. That is, there does not appear to be a dominant orientation or dominant crack population in the sample. Moreover, the data at pressures above 35 MPa indicate that the mineral grain orientations of the Westerly sample are also randomly distributed and the rock is characterized as an isotropic matrix.

Linear Compressibility Data

The linear compressibility data for all the samples are presented in Appendix A, Figures A-1 through A-7 and Table 2. The Katahdin coarse grained granite does not exhibit a dominant crack or mineral grain orientation since the linear compressibilities are the same in each direction (see Appendix A, Figure A-4). However, the linear compressibility data typically suggest that there are dominant pre-existing crack populations for other rocks examined in the study. In particular, the three Soviet samples, the Katahdin fine grained granite, and Sierra White granite exhibit anisotropic linear compressibilities at low pressures. The degree of anisotropy ranges from 40 up to 250%. The typical compressibility anisotropy is 80-100% at low pressures indicating strong dominant crack alignments. It is possible that some of these samples exhibit at least three sets of dominant crack populations which close preferentially over distinct pressure ranges. This is evident when the linear compressibilities as a function of pressure change slopes at different pressure levels.

For example, the altered quartz diorite sample shows a very strong compressibility change at 20 MPa in the 2 direction while those of 1 and 3 change much more gradually and begin to level off at 60 MPa and is depicted in Appendix A, Figure A-1. The set of cracks in the 2 direction closed much more rapidly suggesting that these cracks are more compliant than those in the 1 and 3 directions. Another example of crack alignment anisotropy is clearly shown in the compressibility data for the monzonite sample in Appendix A, Figure A-2. Here all three compressibilities vary differently as a function of pressure and converge to a single value at high pressures. It is interpreted from the data that a minimum of three different sets of crack populations are possible which close at

different pressure levels below 35 MPa. Moreover, the compliance in all three directions is different below 35 MPa. It appears that the compliance of the cracks in the 1 direction is larger than in 2 and in 3, and in 2 larger than in 3. Once the sets of cracks have been closed, the rock matrix appears to be isotropic as indicated by the high pressure data.

Bulk Moduli

The static and dynamic bulk moduli and the compressional and shear wave velocity data are presented in Appendix A, Figures A-1 through A-7 and Table 2. The elastic properties of rocks for small deformations are specified by elastic moduli. The stress-strain ratio under simple hydrostatic pressure gives the static bulk modulus, where:

$$K_s = \frac{\Delta P}{\Delta V / V} = \frac{1}{\beta_1 + \beta_2 + \beta_3} \qquad (5)$$

and V and ΔV are the volume and volume change. For isotropic materials, the dynamic bulk modulus can be computed at a given pressure from compressional and shear wave velocities, V_p and V_s, where:

$$K_d = \rho (V_p^2 - 1.33 V_s^2) \qquad (6)$$

and ρ is the rock density. V_p and V_s are dependent on the mineral properties as well as the crack size, shape, and population density of the sample. The slopes of both V_p and V_s as a function of pressure typically exhibit significant changes up to 35 MPa. As the cracks close, the velocities increase most rapidly with increasing pressure. Once the cracks are closed, the increase in velocity with increasing pressure is relatively small and linear.

Comparison of the static and dynamic bulk moduli gives an indication of the crack

population density and porosity structure. At low pressures the static modulus may be considerably less than the dynamic modulus. The static bulk modulus typically doubles in magnitude for these samples from pressures ranging 5 MPa to 40 MPa, while the dynamic bulk modulus increases only as much as 30% for that range. At 5 MPa, the variance in the static and dynamic moduli ranges from 2% as observed in the Soviet granite sample (Appendix A, Figure A-3; Table 2) and almost 3 : 1 for the altered quartz diorite sample (Appendix A, Figure A-1; Table 2). At pressures higher than 35 MPa the two moduli converge. The moduli variance of the altered quartz diorite is reduced to 50% as the sample is pressurized to 40 MPa. The area bounded by the moduli as a function of pressure is related to the crack size and population density. The larger the area, that is the larger the discrepancy in static and dynamic moduli magnitude, the greater is the crack population density, porosity, and crack size. Both the static and dynamic moduli merge significantly in value above 25 MPa to within a few percent of each other when 50 MPa is reached. At this point, it is most likely that the majority of cracks are completely closed and spherical pores are beginning to collapse. At pressures above 100 MPa the sample is closely represented as a solid material depicting the rock matrix and mineral grain properties solely.

The compilation of data collected for all the samples under hydrostatic loading indicate that the crack populations and crack densities do vary from sample to sample. Moreover, the differences in linear compressibility in the principle directions for certain samples indicate that these samples are anisotropic at low pressures and may exhibit up to few dominant orientations of crack populations. However, at high pressures the data converge to a small range of values. The bulk modulus is typically 15-45 GPa at low pressures and 45-55 GPa at high pressure for all of the granite and crystalline samples studied. Typically, V_p and V_s are slightly faster than 5 and 3 km/sec, respectively, at low pressures; and are 6 and 3.5 km/sec at high pressures. Moreover, like velocities from rock to rock differ by a few percent at low pressures and less than one percent at high pressures.

Water Saturated Measurements

Groundwater is present in subsurface formations at the test sites in the United States and the Soviet Union. Water filled cracks have an effect on seismic velocities. Compressional and shear wave velocities were also measured for these samples saturated

with water during hydrostatic compression tests. These results are shown in Appendix A, Figure A-9. The compressional velocities in the saturated rocks are faster than those for dry conditions while shear wave velocities are slower at low pressures. In particular, the water filled cracks make the rock stiffer. A larger percentage of cracks in the matrix will a greater difference in saturated vs dry velocities. The Soviet granite exhibits more than a 25% variation in V_p at pressures less than 5 MPa but decreases to 10% at the high pressure end. The saturated versus dry sample velocity differences are typically less than 10% for V_p 10% and less than 10% for V_s.

Uniaxial Strain Results

The elastic coefficients were also determined from the stress vs strain data acquired during the uniaxial strain experiments. Values of these coefficients for selected mean stresses are presented in Table 3. The data are also graphically reported in Appendix B, Figures B-1 through B-7. The boundary conditions of the uniaxial strain experiments are fundamentally different from those of the hydrostatic compression experiments. In the uniaxial strain experiments the displacements on the surface of the cylindrical specimen are prescribed. An axial displacement is applied on the end of the specimen while the radial strain is maintained constant. Consequently, the stress in the axial direction, σ_1, differs form the stresses in the radial direction, σ_2 and σ_3. Here σ_2 and σ_3 are equal and the radial strains, ε_2 and ε_3 are held constant while ε_1 is varied.

The linear compressibility data suggest that the rock properties of the crystalline samples appear isotropic at high pressure. Since these properties are isotropic then the results for these experiments would be the same regardless of the core orientation. The set of dynamic moduli are computed in the same fashion for the uniaxial strain experiments as in the hydrostatic compression test. The static moduli, the stiffness C_{ijkl}, are determined for these boundary conditions. Static and dynamic moduli are compared include the (1) shear modulus, (2) bulk modulus, (3) Young's modulus and (4) Poisson's ratio. These moduli are described in detail in Sheriff [1976] and are given below:

(1) Shear Modulus, G

$$G_s = (\Delta\sigma_1 - \Delta P) / 2\,\Delta\varepsilon_1 \qquad (7)$$

$$G_d = \rho\, V_s^2 \qquad (8)$$

Where G_s and G_d are the static and dynamic shear moduli, $\Delta\sigma_1$ is the change in axial stress, ΔP is the confining pressure change ($\Delta P = \Delta\sigma_1 = \Delta\sigma_1$) and $\Delta\varepsilon_1$ is the axial strain change.

(2) Bulk Modulus, K

$$K_s = \frac{\Delta\sigma_m}{\Delta\varepsilon_1} \qquad (9)$$

$$K_d = \rho\, V_p^2 - G_d \qquad (10)$$

where σ_m is the mean stress and $\sigma_m = \sigma_1 + \sigma_2 + \sigma_3 = \sigma_1 + 2P$

(3) Young's Modulus, E

$$E_s = \frac{9\,K_s G_s}{3K_s + G_s} \qquad (11)$$

$$E_d = \frac{9\,K_d G_d}{3K_d + G_d} \qquad (12)$$

(4) Poisson's Ratio, ν

$$\nu_s = \frac{3K_s - 2G_s}{6K_s + 2G_s} \tag{13}$$

$$\nu_d = \frac{3K_d - 2G_d}{6K_d + 2G_d} \tag{14}$$

The like moduli determined from the uniaxial strain experiments agree closely for all the crystalline rocks.The moduli for both Katahdin granites (Appendix B, Figures B-4 and B-5) reflect the typical properties for all the specimens as a function of uniaxial stress. The largest changes with load are observed in the bulk and Young's moduli over the loading cycle. Both these moduli are strongly dependent on the axial stress and strain. Moreover, the compressional wave velocity is also greatly affected by axial changes. The bulk modulus typically ranges 20 GPa to 55 GPa while Young's modulus ranges 35 GPa to 85 GPa over the loading cycle. The compressional wave velocity varies from 5.6 to 6.1 km/sec from low to high stresses. The variation in the bulk modulus at low stresses between samples is roughly within 10 percent. However, the contrast between the altered quartz diorite sample (Appendix B, Figure B-1) and Westerly granite (Appendix B, Figure B-6) is approximately 1 : 2 at low pressures. This difference is most likely attributed to the crack population and alignment present at low stresses. The higher moduli indicate a stiffer matrix with higher aspect ratio cracks. As with the hydrostatic compression experiments, at high stresses in uniaxial strain, the influence of low aspect ratio cracks is minimal, and the moduli vary by only a few percent from rock to rock. For example, the difference in bulk moduli between the altered quartz diorite and Westerly granite is within 2 percent at higher pressures.

As in the hydrostatic experiments, the static moduli are more sensitive to stress and pressure changes than dynamic moduli. This effect is apparent in the stress sensitivity of Young's modulus. At low stresses, the altered quartz diorite sample and Westerly granite moduli differ by 1 : 3 and this difference diminishes to less than 30 percent at high stress.

The dynamic Young's moduli vary 20 percent at low pressures and less than 2 percent at high stresses.

Next, the shear modulus, shear velocities, and Poisson's ratio were examined. The nature of the uniaxial strain experiment minimizes shear slip since the radial strain is held constantly at zero. Variations in shear are greatest at low pressures and non-linear changes are dependent on the crack populations. The altered quartz diorite and Westerly shear moduli differ approximately 1 : 3 at low pressures and diminish to slightly more than 30 percent at high pressures; similarly to the other moduli. Poisson's ratio remains nearly constant over the loading cycle. However, the effects of the crack populations are seen in the static Poisson's ratio at low pressures and appear smaller than the other measurements. Poisson's ratio is consistent from rock to rock and may very within a few percent at any given pressure. The largest differences are in the Poisson's ratio data are noted between ν_s and ν_d. The variation is several percent at any stress state.

CONCLUSIONS

The elastic properties determined from the static and dynamic measurements during hydrostatic compression and uniaxial strain have been compared. An analysis of the data suggest that:

(1) The mineralogy of these crystalline rocks are very similar. The like elastic moduli for these rocks are comparable in magnitude and vary within a few percent from sample to sample.

(2) The rock matrix properties appear to be isotropic, especially at high pressures and stresses. However, a degree of anisotropy is present for certain samples at low pressures.

(3) The degree of anisotropy may vary from specimen to specimen at low pressures. The degree of anisotropy is greatly diminished at high pressures to less than 10 percent. The low pressure anisotropy is predominantly dependent on the crack populations and their alignments.

(4) The static measurements are more sensitive to pressure and stress changes than the dynamic measurements. Static moduli are consistently smaller than dynamic moduli and the like moduli merge at high pressures. The area bounded by like static and dynamic moduli is dependent on the porosity and crack structure in the rock matrix. This area is much smaller for crystalline rocks compared to more porous sandstones. The differences in static and dynamic moduli are not fully understood.

FUTURE STUDIES

Further experiments of this type will be performed on saturated samples. Groundwater is present in the test areas and has a significant effect on the elastic properties of the *in situ* rocks and seismic velocity. Water filled cracks will make the rock stiffer.

An important parameter would be to investigate is the percent water saturation for these experiment types. In addition, it would be worthwhile to measure the elastic properties while fluid is flowing through the samples. A seismic point source would initiate fluid flow in saturated rocks in the vicinity of the source. Lastly, models of crack populations, crack sizes, water saturation, and related effects should be considered.

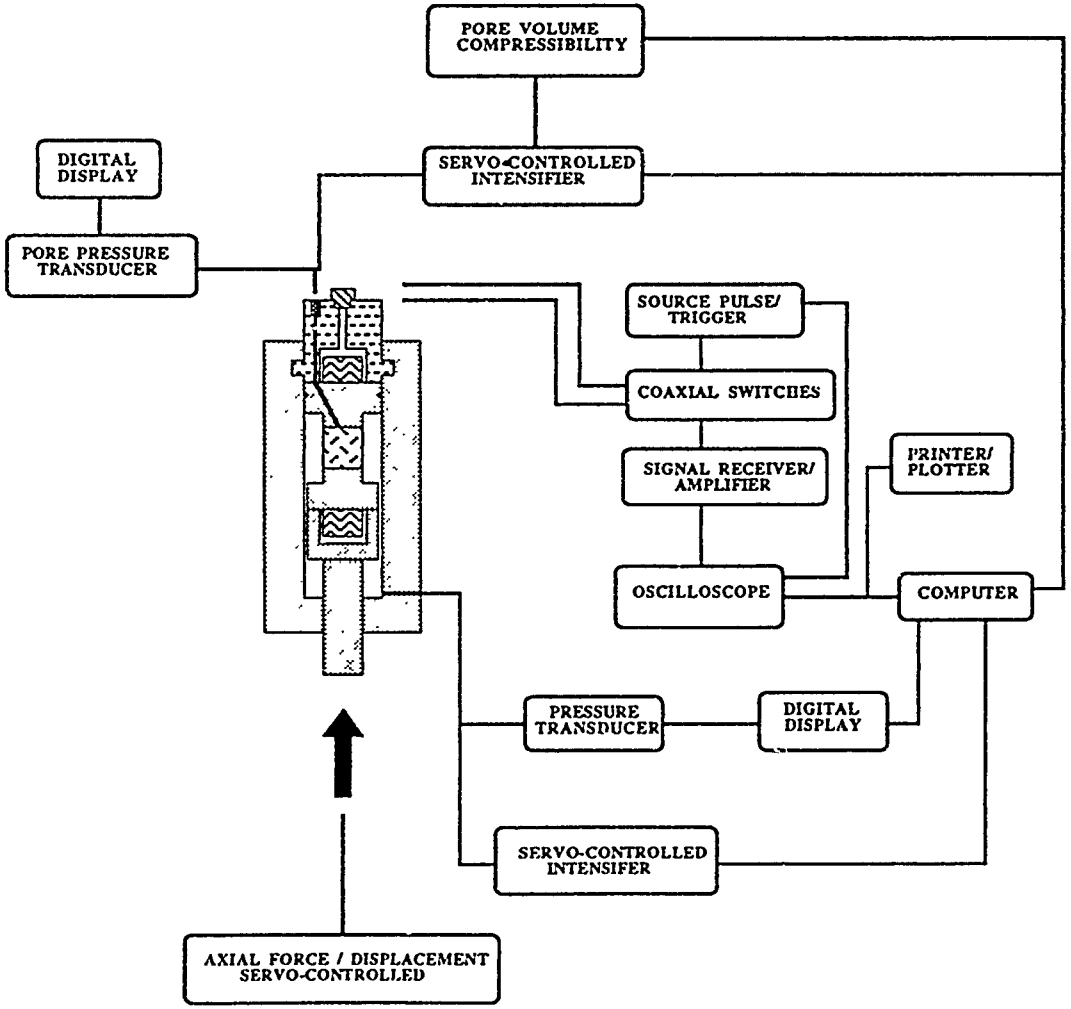

Figure 1. Schematic diagram of the experimental apparatus for ultrasonic velocity and attenuation measurements as a function of pressure.

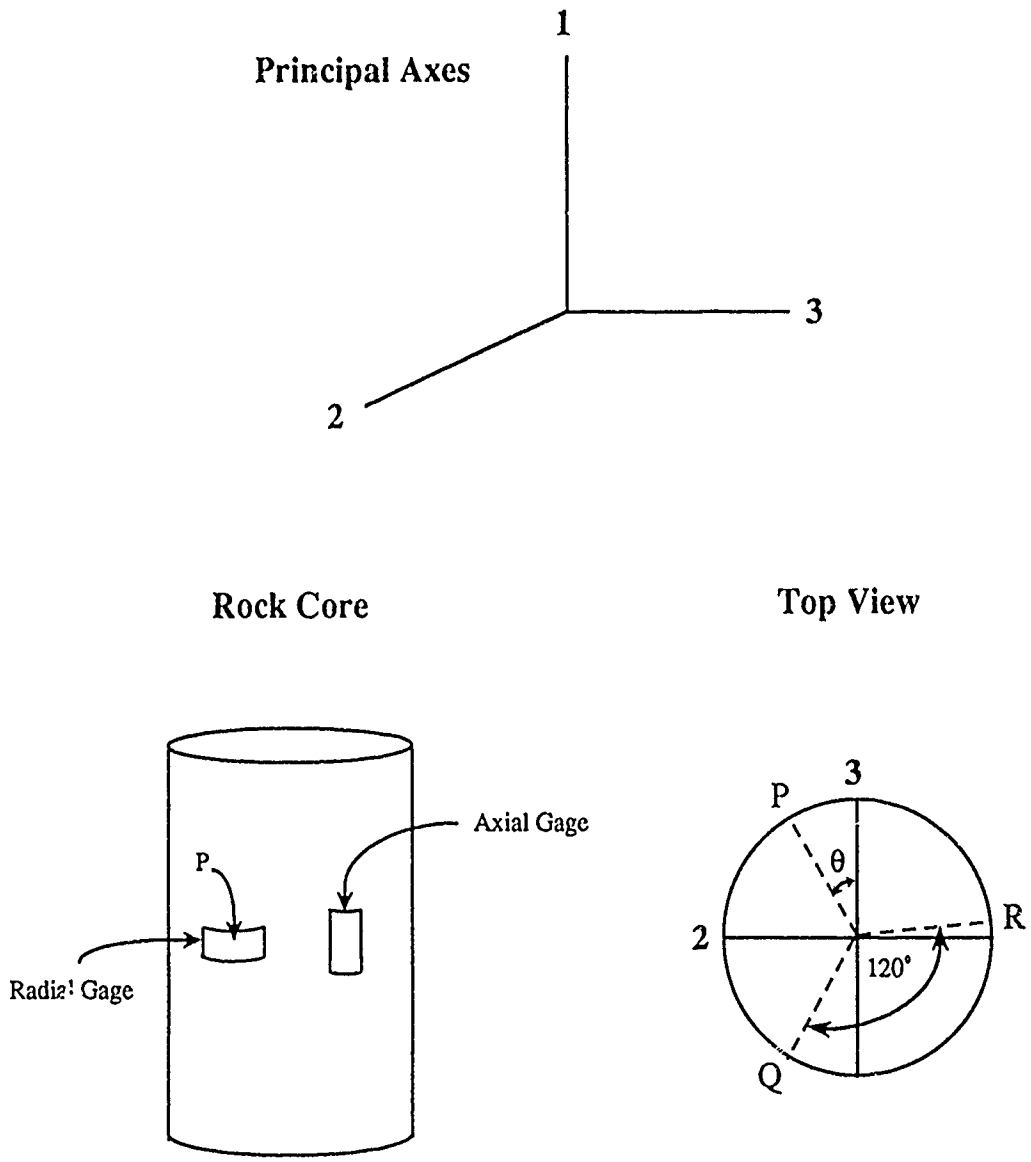

Figure 2. Schematic diagram showing the core orientation relative to the the principle directions, 1, 2, 3 and the placement of strain gages

TABLE 1

Altered Quartz Diorite

Bulk Density: 2.687 g/cm^3
Porosity: 1.1%
Mean Grain Diameter: 0.40mm
Composition:

Plagioclase	48%
Biotiie	17%
Quartz	12%
Sericite	20%
Opaques	2%

Monzonite

Bulk Density: 2.671 g/cm^3
Porosity: 1.8%
Mean Grain Diameter: 0.48 mm
Composition:

Microcline	41%
Albite	22%
Quartz	10%
Apatite	9%
Biotite	8%

Granite

Bulk Density: 2.573 g/cm^3
Porosity: 1.9%
Mean Grain Diameter: 0.96 mm
Composition:

Perthite	46%
Quartz	25%
Albite	13%
Biotite	8%
Apaptite	6%
Zircon	2%

Granite Mt. Katahdin, Maine

Fine Grained (NGL)
Bulk Denstiy: 2.635 g/cm^3
Porosity: 0.7%
Mean Grain Diameter: 0.71mm
Compostion:

Microline	51%
Quartz	27%
Albite	8%
Biotite	12%
Opaque	2%

Granite, Mt. Katahdin, Maine

Coarse Grained (KGL)
Bulk Density: 2.615 g/cm^3
Porosity: 1.2%
Mean Grain Diameter: 1.04 mm
Compostition:

Microcline	45%
Quartz	34%
Albite	9%
Opaque	2%

Granite, (Sierra White), California

Bulk Density: 2.638 g/cm^3

Porosity: 0.9%

Mean Grain Diameter: 0.70 mm

Composition:

Microcline	44%
Quartz	38%
Albite	2%
Biotite	11%
Muscovite	5%

Granite, Westerly, Rhode Island

Bulk Density: 2.646 g/cm^3

Porosity: 0.9%

Mean Grain Diameter: 0.75 mm

Composition:

Microcline	35%
Quartz	28%
Albite	31%
Mica	5%

TABLE 2

STATIC and DYNAMIC BULK MODULI
MEASURED DURING HYDROSTATIC COMPRESSION
(GPa)

	5 MPa		40 MPa		100 MPa	
	STATIC	DYNAMIC	STATIC	DYNAMIC	STATIC	DYNAMIC
Semipalatinsk Region, USSR						
Altered Quartz Diorite	13.80	42.02	30.89	47.06	44.11	51.25
Monzonite	19.98	41.29	35.92	44.13	48.85	50.46
Granite	19.31	19.74	35.50	33.03	44.95	
Katahdin Granites						
Coarse grained	21.07	37.81	37.35	46.85	49.18	50.59
Fine grained	20.62	53.14	52.13	54.49	59.02	54.55
Westerly Granite	28.49	41.49	46.78	50.48	54.05	51.45
Sierra White Granite	17.81	38.61	38.09	47.59	49.88	51.59
Berea Sandstone	9.05	9.62	14.87	15.73	16.60	17.48

COMPRESSIONAL AND SHEAR WAVE VELOCITIES
(km/sec)

	5 MPa		40 MPa		100 MPa	
	Vp	Vs	Vp	Vs	Vp	Vs
Semipalatinsk Region, USSR						
Altered Quartz Diorite	5.608	3.246	5.803	3.394	6.104	3.495
Monzonite	5.378	3.135	5.795	3.332		
Granite	4.203	2.778	5.202	3.247		
Katahdin Granites						
Coarse grained	5.201	3.078	5.768	3.418	6.036	3.569
Fine grained	5.903	3.297	6.009	3.377	6.081	3.486
Westerly Granite	5.407	3.190	5.915	3.449	6.022	3.543
Sierra White Granite	5.231	3.088	5.812	3.434	6.059	3.585
Berea Sandstone	3.269	2.174	3.945	2.511	4.117	2.598

TABLE 2

LINEAR COMPRESSIBILITIES
MEASURED DURING HYDROSTATIC COMPRESSION
(1/GPA) X 10E-2

	5 MPa			40 MPa			100 MPa		
	β1	β2	β3	β1	β2	β3	β1	β2	β3
Semipalatinsk Region, USSR									
Altered Quartz Diorite	2.60	1.72	3.22	1.18	0.67	1.44	0.84	0.51	0.91
Monzonite	2.41	1.47	1.17	1.12	0.82	0.85	0.73	0.65	0.67
Granite	2.57	1.00	2.59	1.38	0.50	1.15	0.98	0.48	0.80
Katahdin Granites									
Coarse grained	1.54	1.41	1.62	0.94	0.78	0.93	0.76	0.60	0.67
Fine grained	2.45	1.13	1.26	0.73	0.56	0.62	0.54	0.56	0.59
Westerly Granite	1.34	1.11	1.18	0.77	0.70	0.64	0.67	0.64	0.52
Sierra White Granite	2.28	1.84	1.63	0.93	0.81	0.88	0.69	0.63	0.68

TABLE 3

STATIC and DYNAMIC MODULI
MEASURED DURING UNIAXIAL STRAIN LOADING

BULK MODULUS
(GPa)

	5 MPa		40 MPa		125 MPa	
	STATIC	DYNAMIC	STATIC	DYNAMIC	STATIC	DYNAMIC
Semipalatinsk Region, USSR						
Altered Quartz Diorite	17.05		44.47		58.86	
Monzonite	23.47		45.24		57.82	
Granite	21.57		39.06			
Katahdin Granites						
Coarse grained	24.71	48.54	40.99	53.84	44.59	56.22
Fine grained		52.39	49.40	54.97	55.76	58.18
Westerly Granite	34.58	46.91	51.40	51.77	57.64	53.86
Sierra White Granite	17.97	46.26	44.06	52.45	55.94	53.65

YOUNG'S MODULUS
(GPa)

	5 MPa		40 MPa		125 MPa	
	STATIC	DYNAMIC	STATIC	DYNAMIC	STATIC	DYNAMIC
Semipalatinsk Region, USSR						
Altered Quartz Diorite	22.71		55.78		64.51	
Monzonite	44.07		70.48		76.08	
Granite	38.59		65.82		65.88	
Katahdin Granites						
Coarse grained	52.91	68.84	69.29	77.62	72.71	81.40
Fine grained		67.12	72.76	75.44	78.31	79.69
Westerly Granite	65.59	73.97	87.85	80.87	90.68	84.08
Sierra White Granite	35.77	63.62	72.41	76.75	79.65	82.46

TABLE 3

STATIC and DYNAMIC MODULI
MEASURED DURING UNIAXIAL STRAIN LOADING

SHEAR MODULUS
(GPa)

	5 MPa		40 MPa		125 MPa	
	STATIC	DYNAMIC	STATIC	DYNAMIC	STATIC	DYNAMIC
Semipalatinsk Region, USSR						
Altered Quartz Diorite	8.89		21.60		24.48	
Monzonite	18.56		28.41		29.70	
Granite	16.06		27.00		26.06	
Katahdin Granites						
Coarse grained	23.14	27.24	28.44	30.81	29.60	32.34
Fine grained		26.09	29.00	29.67	30.93	31.33
Westerly Granite	27.70	29.89	36.15	32.62	36.63	33.91
Sierra White Granite	15.31	25.03	29.53	30.55	31.54	33.13

POISSON'S RATIO

	5 MPa		40 MPa		125 MPa	
	STATIC	DYNAMIC	STATIC	DYNAMIC	STATIC	DYNAMIC
Semipalatinsk Region, USSR						
Altered Quartz Diorite	0.28		0.29		0.32	
Monzonite	0.19		0.24		0.28	
Granite	0.20		0.22		0.26	
Katahdin Granites						
Coarse grained	0.14	0.26	0.22	0.26	0.23	0.26
Fine grained		0.29	0.27	0.27	0.27	0.27
Westerly Granite	0.18	0.24	0.22	0.24	0.24	0.24
Sierra White Granite	0.17	0.27	0.23	0.26	0.26	0.24

TABLE 3

COMPRESSIONAL AND SHEAR WAVE VELOCITIES
MEASURED DURING UNIAXIAL STRAIN LOADING
(km/sec)

	5 MPa		40 MPa		125 MPa	
	Vp	Vs	Vp	Vs	Vp	Vs
Semipalatinsk Region, USSR						
Altered Quartz Diorite						
Monzonite						
Granite						
Katahdin Granites						
Coarse grained	5.695	3.226	6.023	3.431	6.161	3.515
Fine grained	5.749	3.145	5.987	3.354	6.157	3.447
Westerly Granite	5.739	3.368	6.013	3.518	6.132	3.587
Sierra White Granite	5.486	3.076	5.934	3.398	6.081	3.540

APPENDIX A

HYDROSTATIC COMPRESSION RESULTS

SOVIET SAMPLE (ALTERED QUARTZ DIORITE)

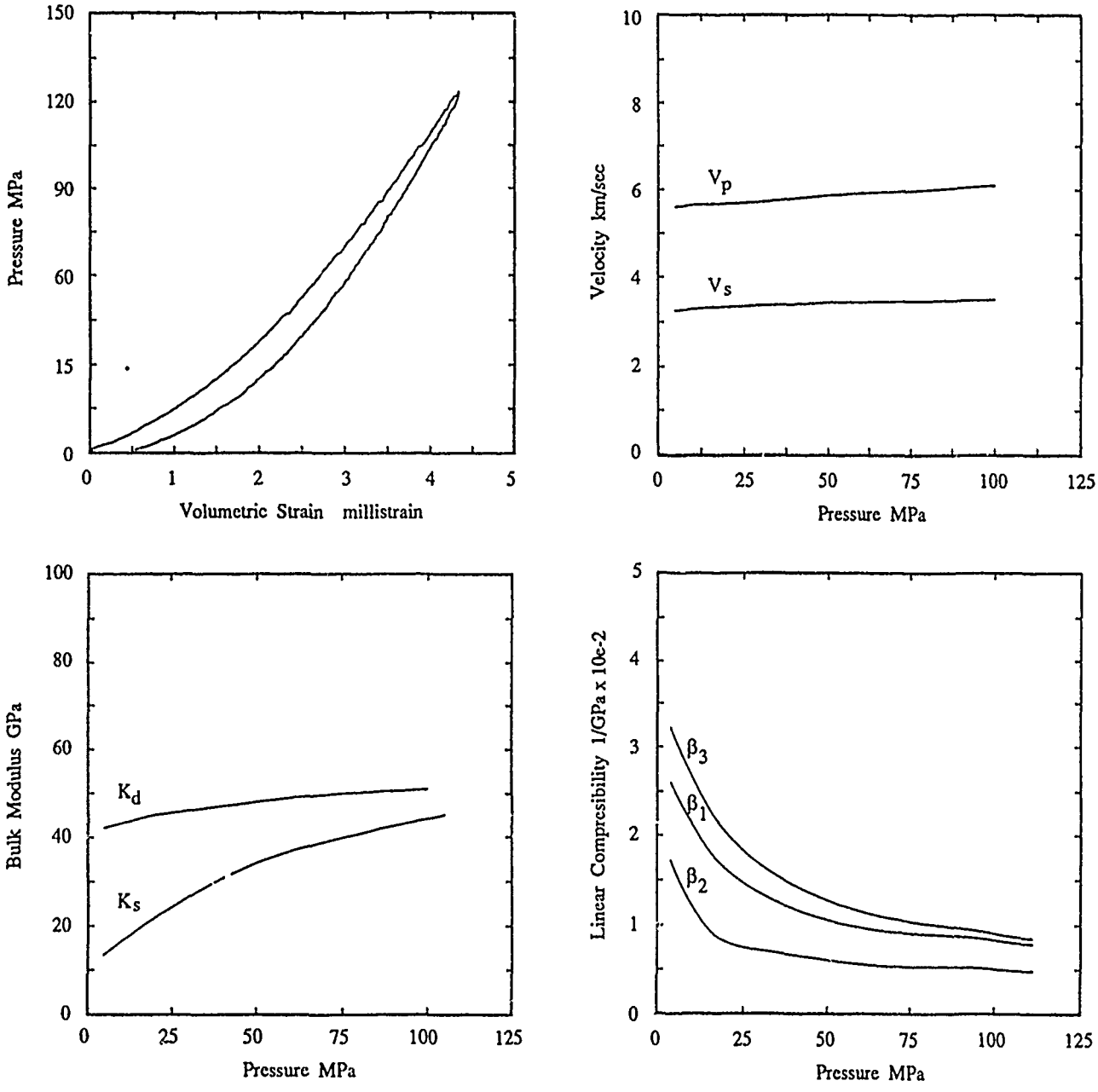

Figure A-1 Hydrostatic compression experimental data for altered quartz diorite sample obtained from surface outcrop located near the northwest corner of the test site near Semipalatinsk, USSR.

SOVIET SAMPLE (MONZONITE)

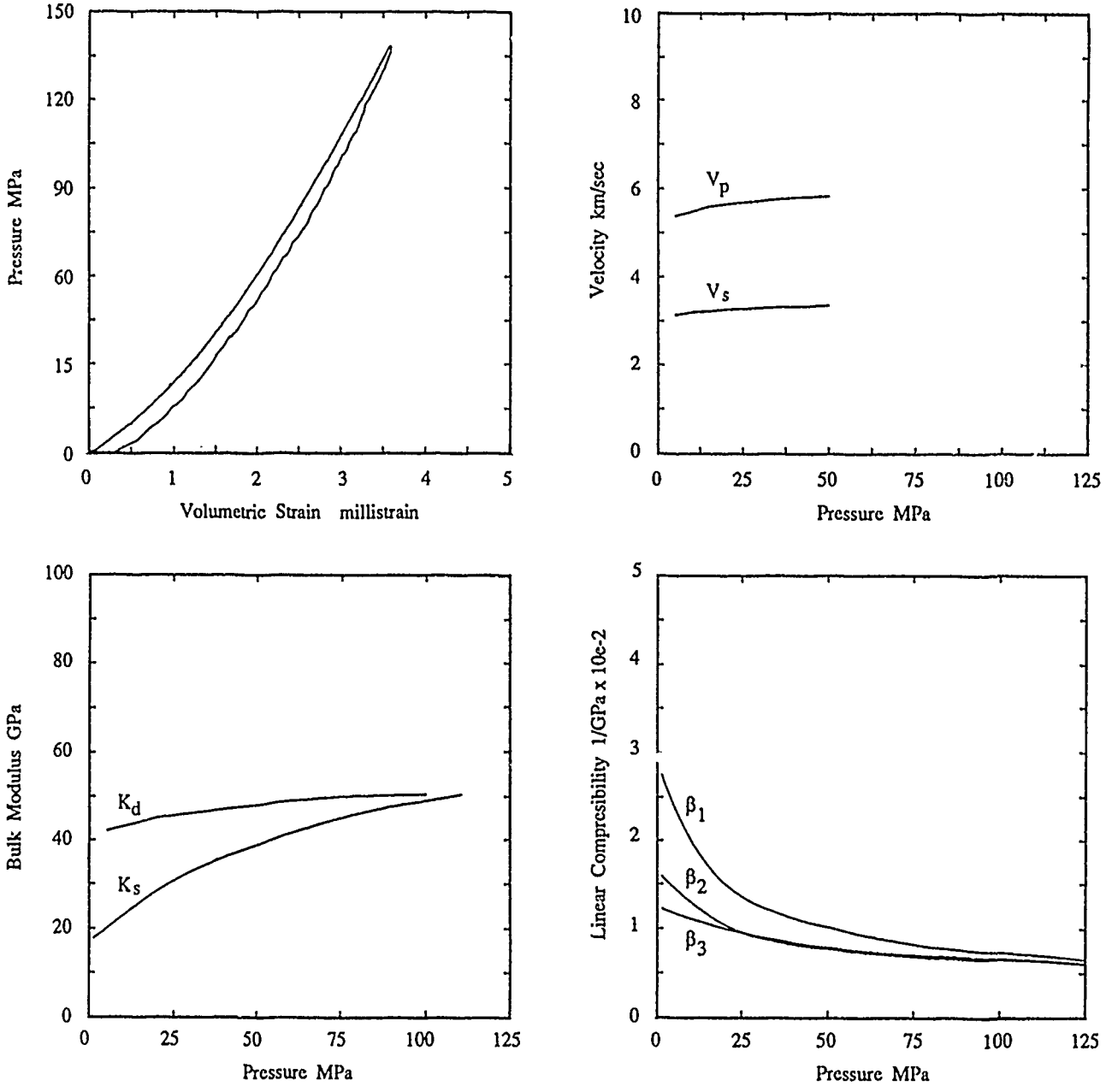

Figure A-2 Hydrostatic compression experimental data for monzonite sample obtained from surface outcrop located near the northwest corner of the test site near Semipalatinsk, USSR.

SOVIET SAMPLE (GRANITE)

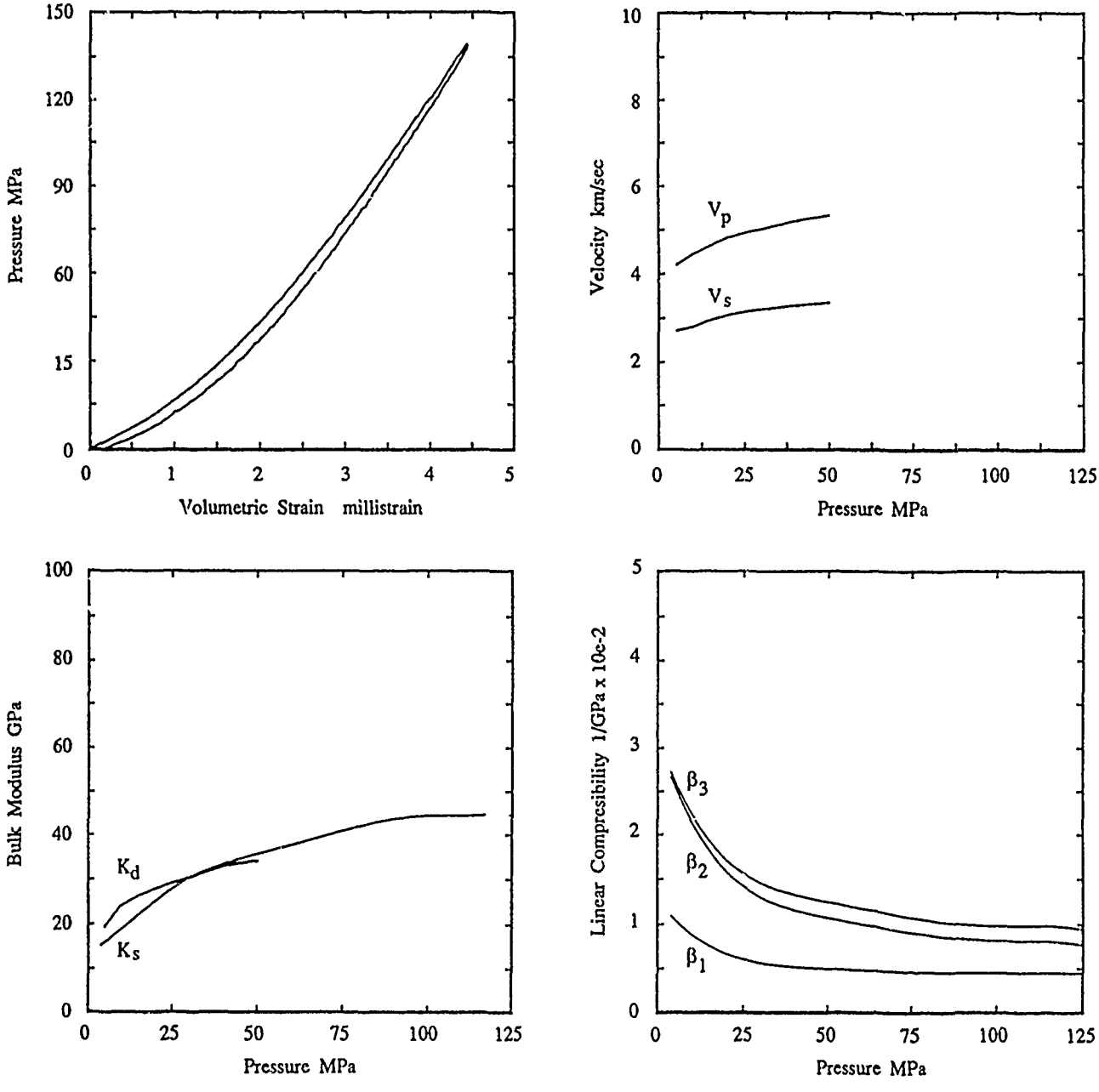

Figure A-3 Hydrostatic compression experimental data for granite sample obtained at a depth of 34 meters from an NRDC borehole located south of the test site near Semipalatinsk, USSR.

KATAHDIN GRANITE (COARSE GRAINED)

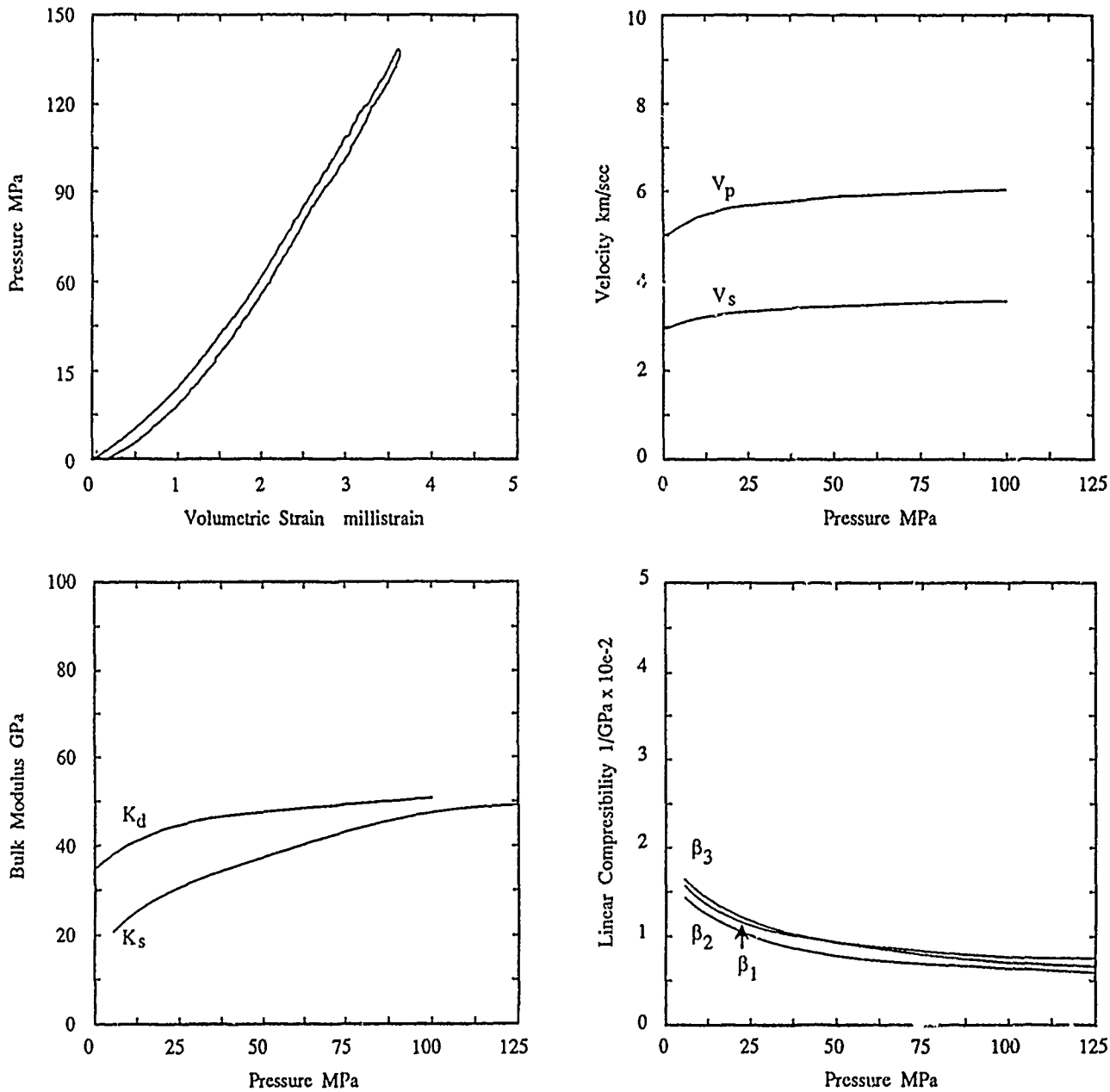

Figure A-4 Hydrostatic compression experimental data for coarse grained granite sample obtained from surface outcrop located near Mt. Katahdin, Maine.

KATAHDIN GRANITE (FINE GRAINED)

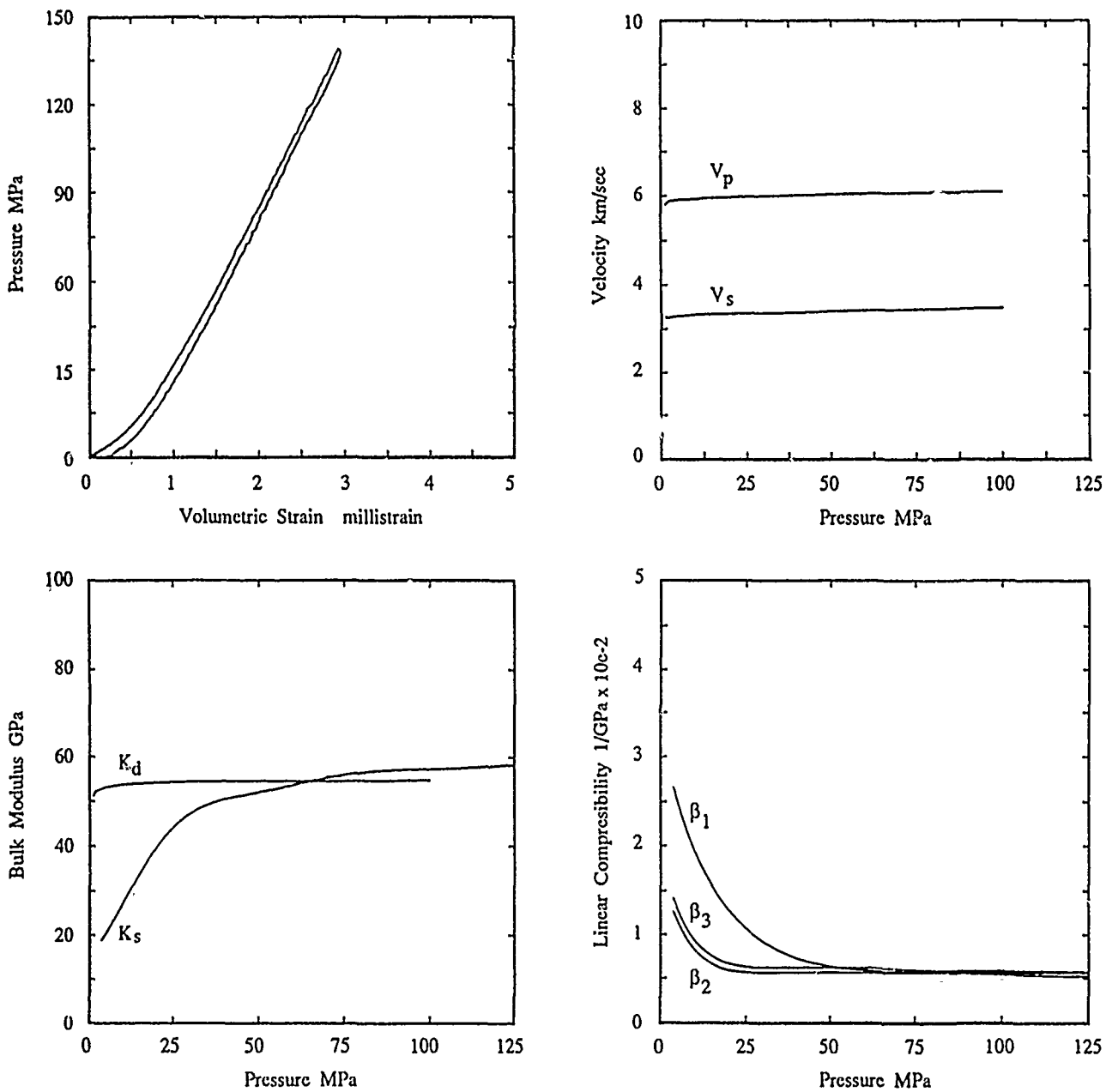

Figure A-5 Hydrostatic compression experimental data for fine grained granite sample obtained from surface outcrop located near Mt. Katahdin, Maine.

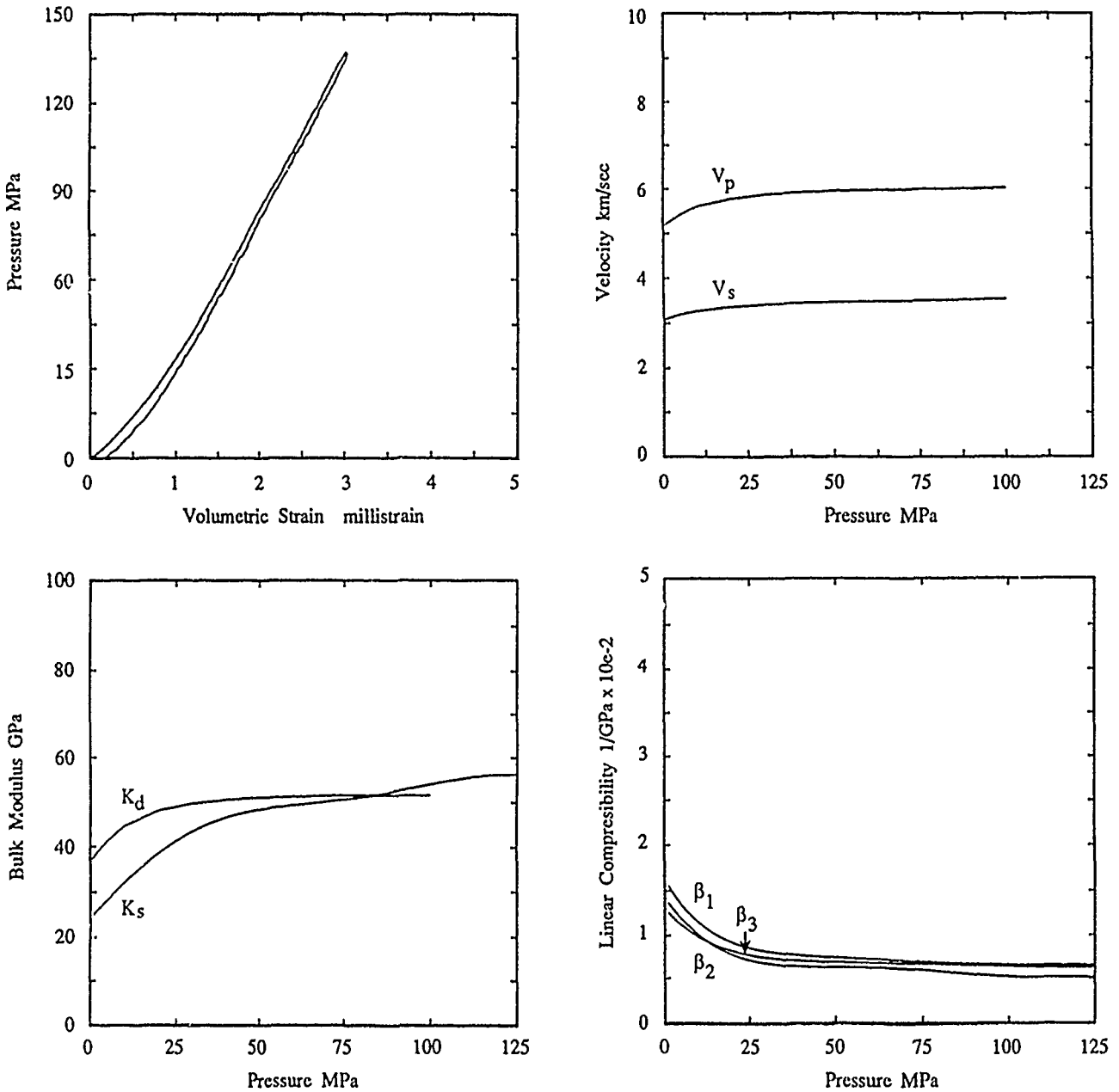

Figure A-6 Hydrostatic compression experimental data for Westerly Granite sample obtained from surface outcrop from Westery, Rhode Island.

SIERRA WHITE GRANITE

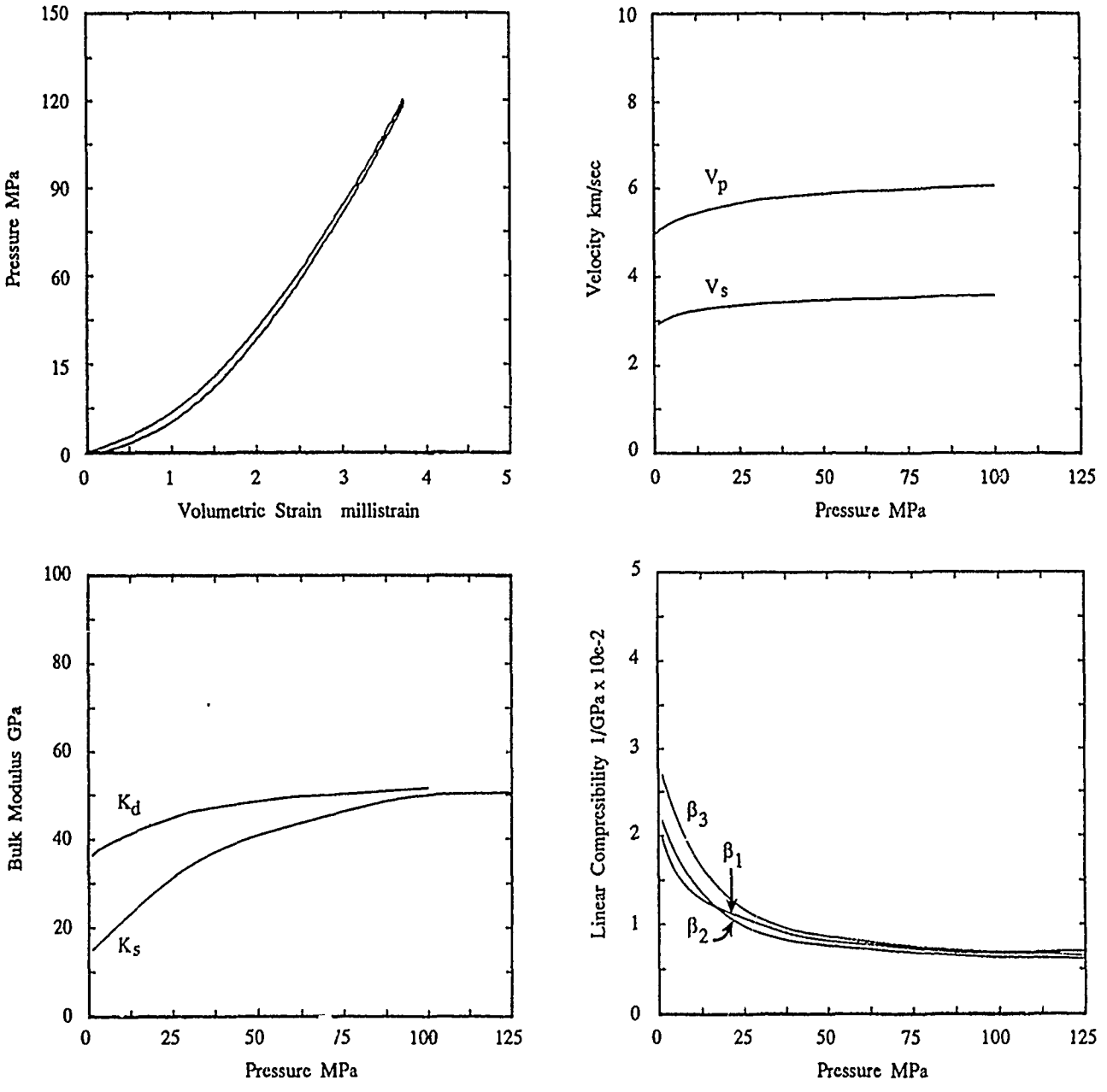

Figure A-7 Hydrostatic compression experimental data for Sierra White Granite sample obtained from surface outcrop from Raymond, California.

HYDROSTATIC COMPRESSION
BEREA SANDSTONE

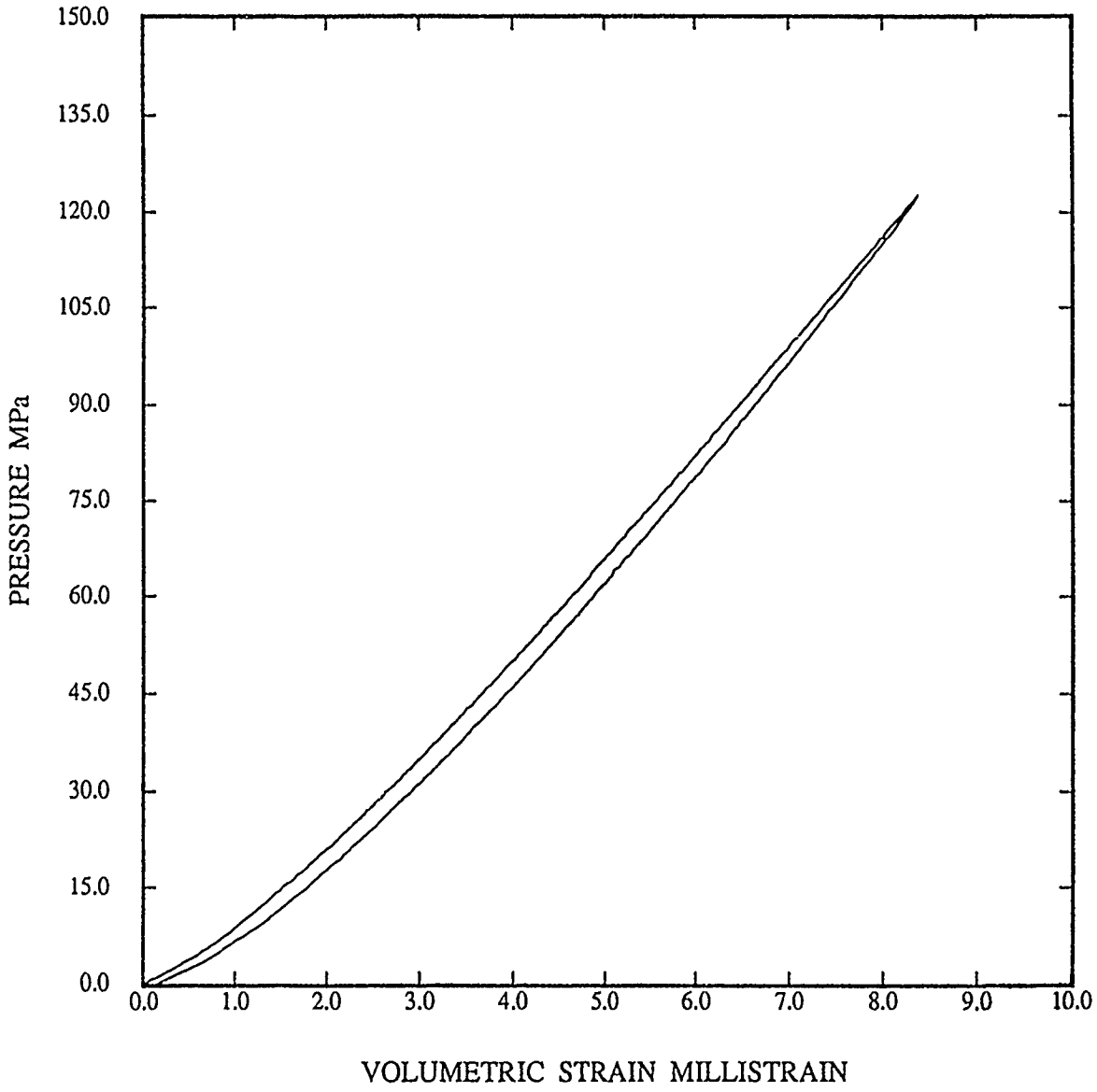

Figure A-8

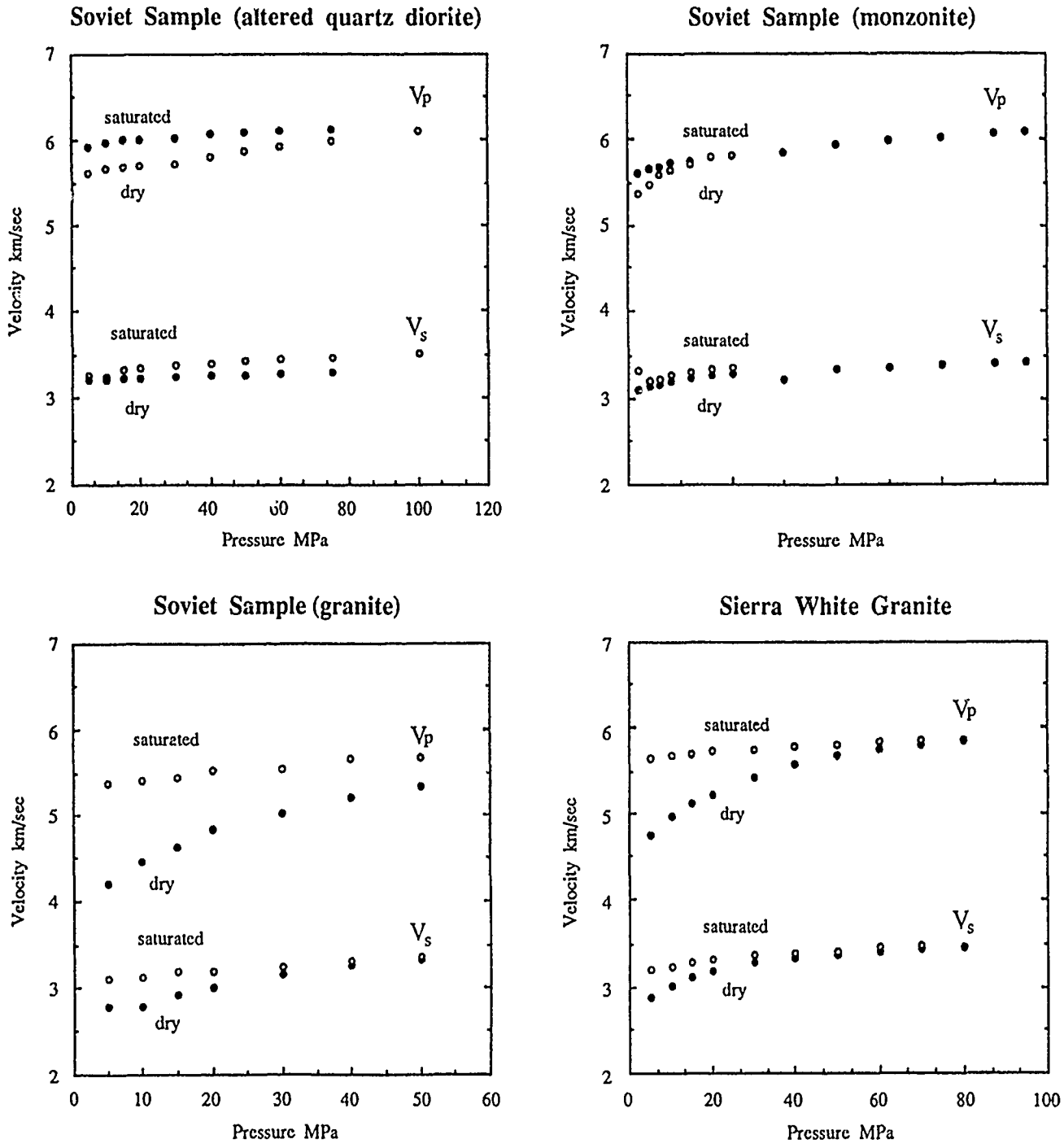

Figure A-9 Comparison of dry and water saturated samples and their compressional and shear wave velocities for the Soviet rocks obtained near the test site near Semipalatinsk, USSR and Sierra White Granite.

APPENDIX B

UNIAXIAL STRAIN RESULTS

SOVIET SAMPLE (ALTERED QUARTZ DIORITE)

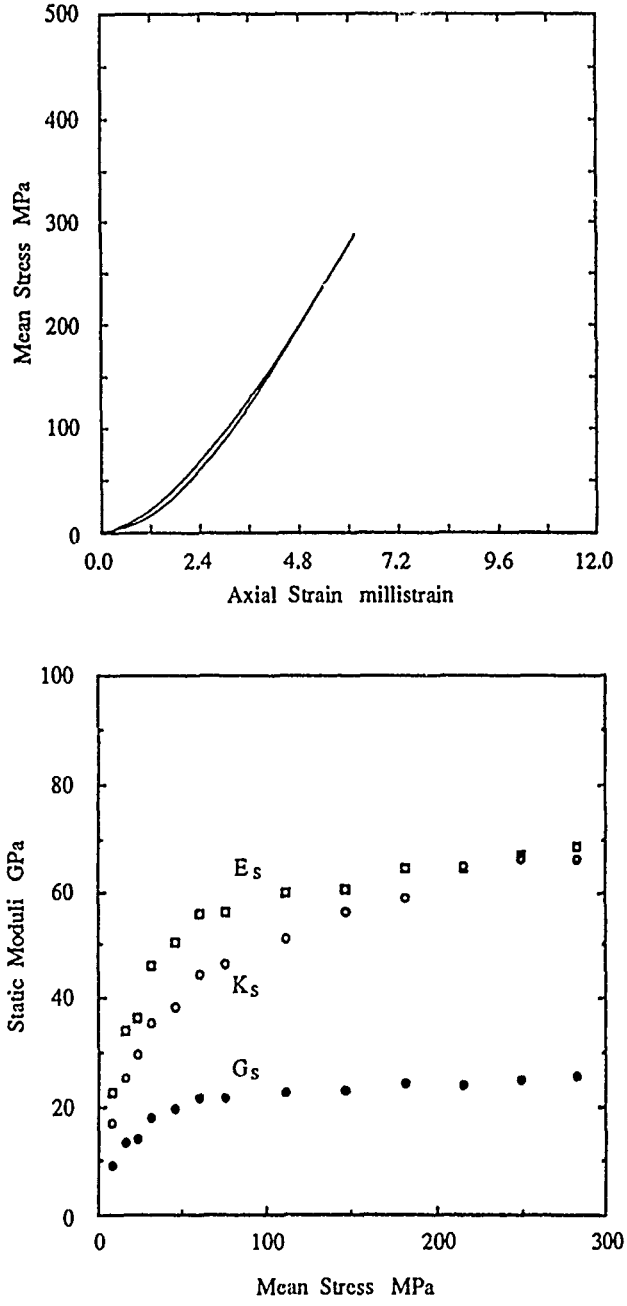

Figure B-1 Uniaxial strain experimental data for altered quartz diorite sample obtained from surface outcrop located near the northwest corner of the test site near Semipalatinsk, USSR.

SOVIET SAMPLE (MONZONITE)

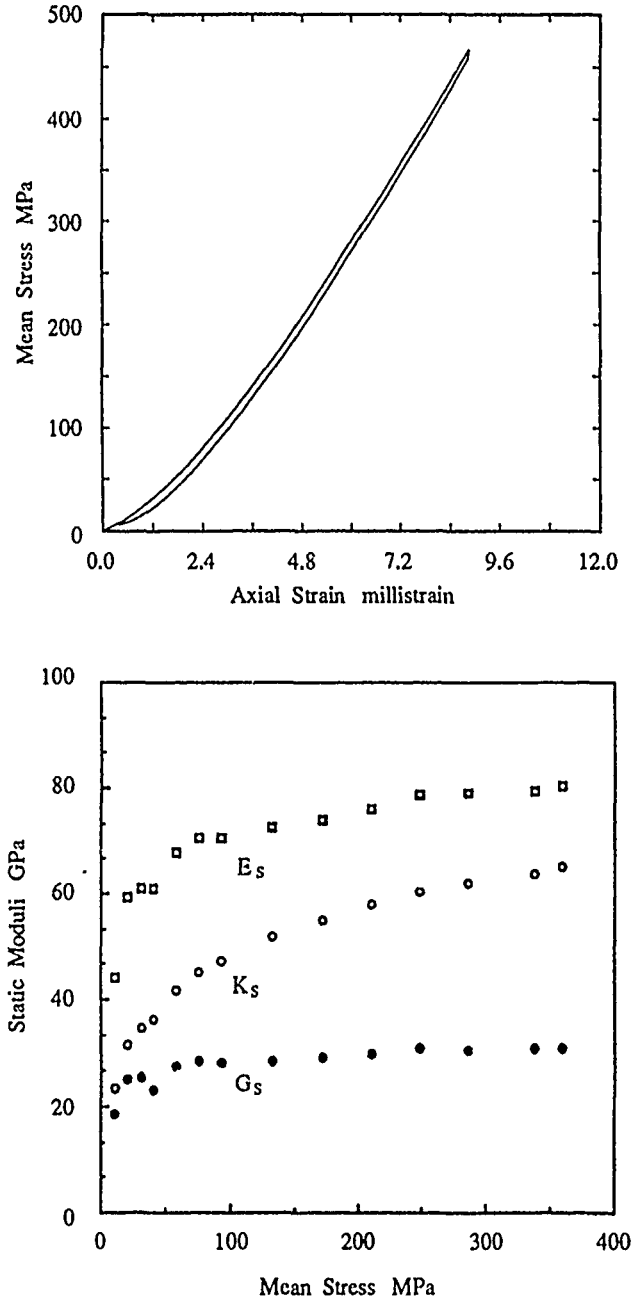

Figure B-2 Uniaxial strain experimental data for monzonite sample obtained from surface outcrop located near the northwest corner of the test site near Semipalatinsk, USSR.

SOVIET SAMPLE (GRANITE)

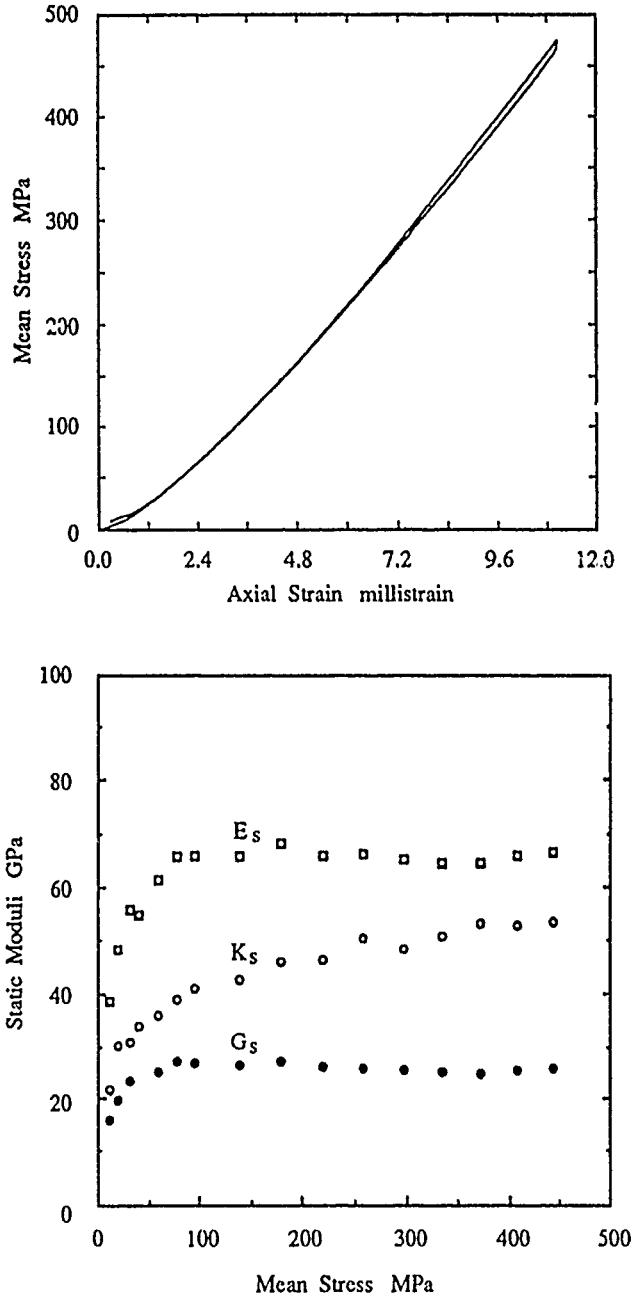

Figure B-3 Uniaxial strain experimental data for granite sample obtained at a depth of 34 meters from an NRDC borehole located south of the test site near Semipalatinsk, USSR.

KATAHDIN GRANITE (COARSE GRAINED)

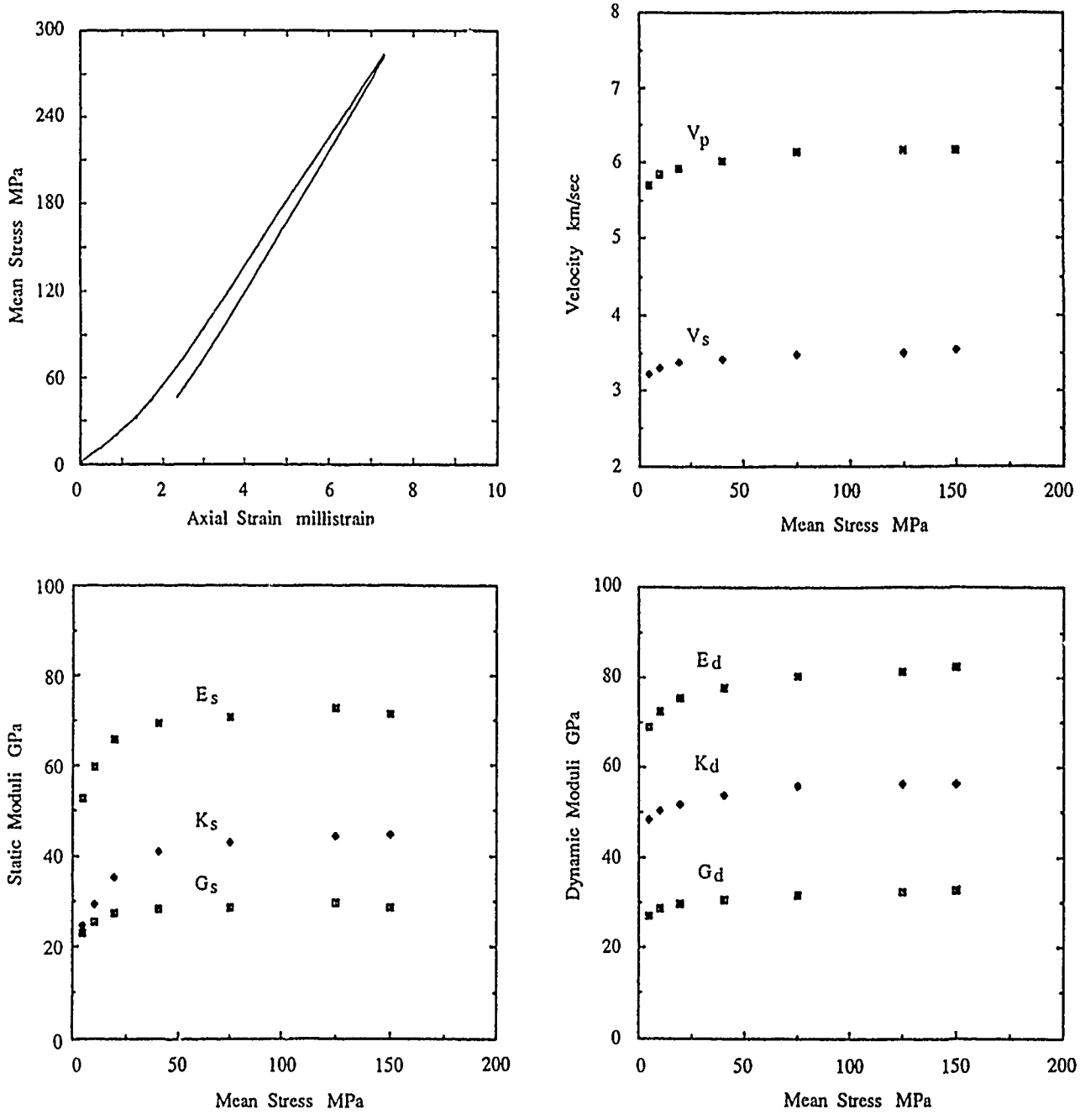

Figure B-4 Uniaxial strain experimental data for coarse grained granite sample obtained from surface outcrop located near Mt. Katahdin, Maine.

KATAHDIN GRANITE (FINE GRAINED)

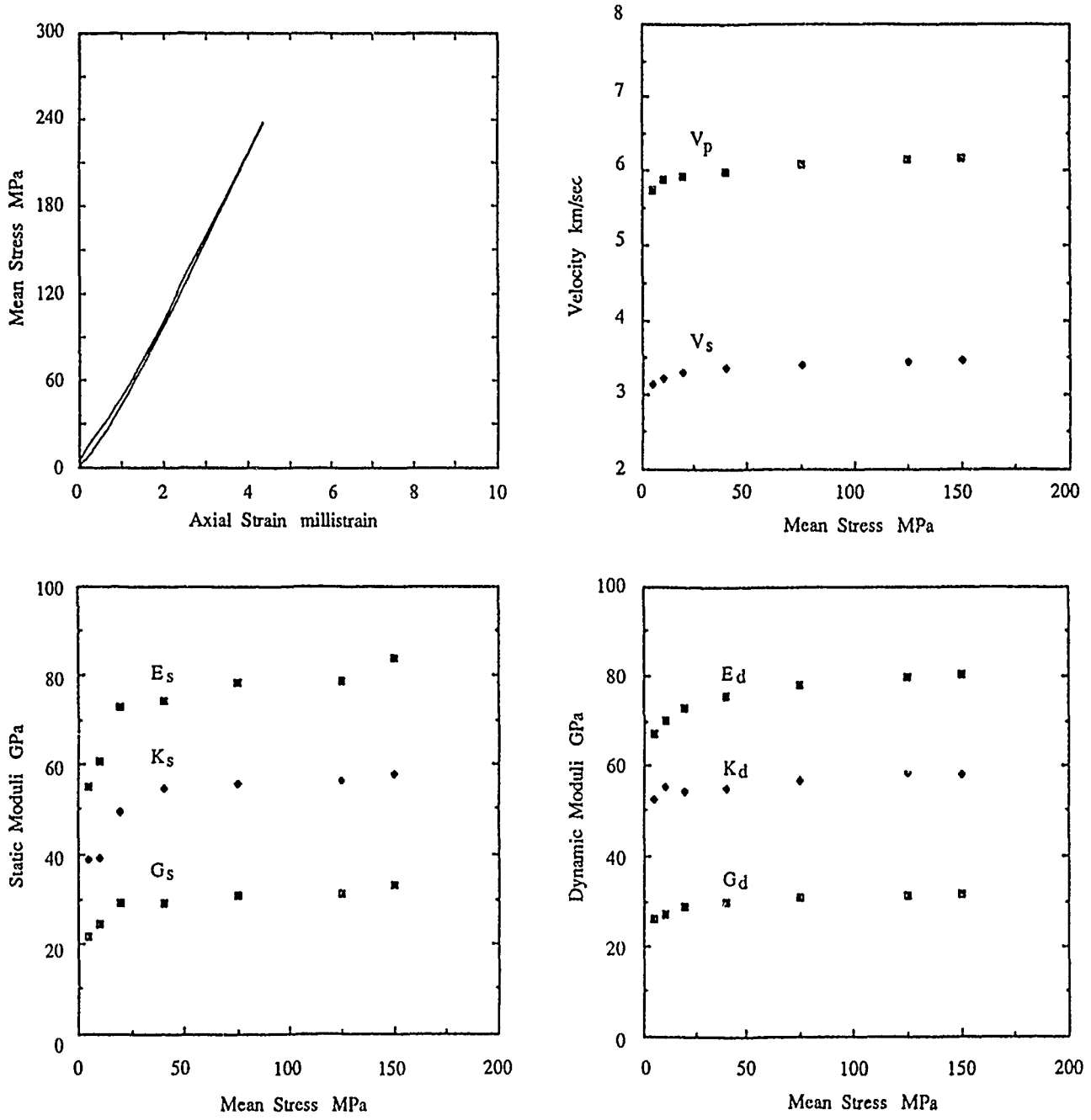

Figure B-5 Uniaxial strain experimental data for fine grained granite sample obtained from surface outcrop located near Mt. Katahdin, Maine.

WESTERLY GRANITE

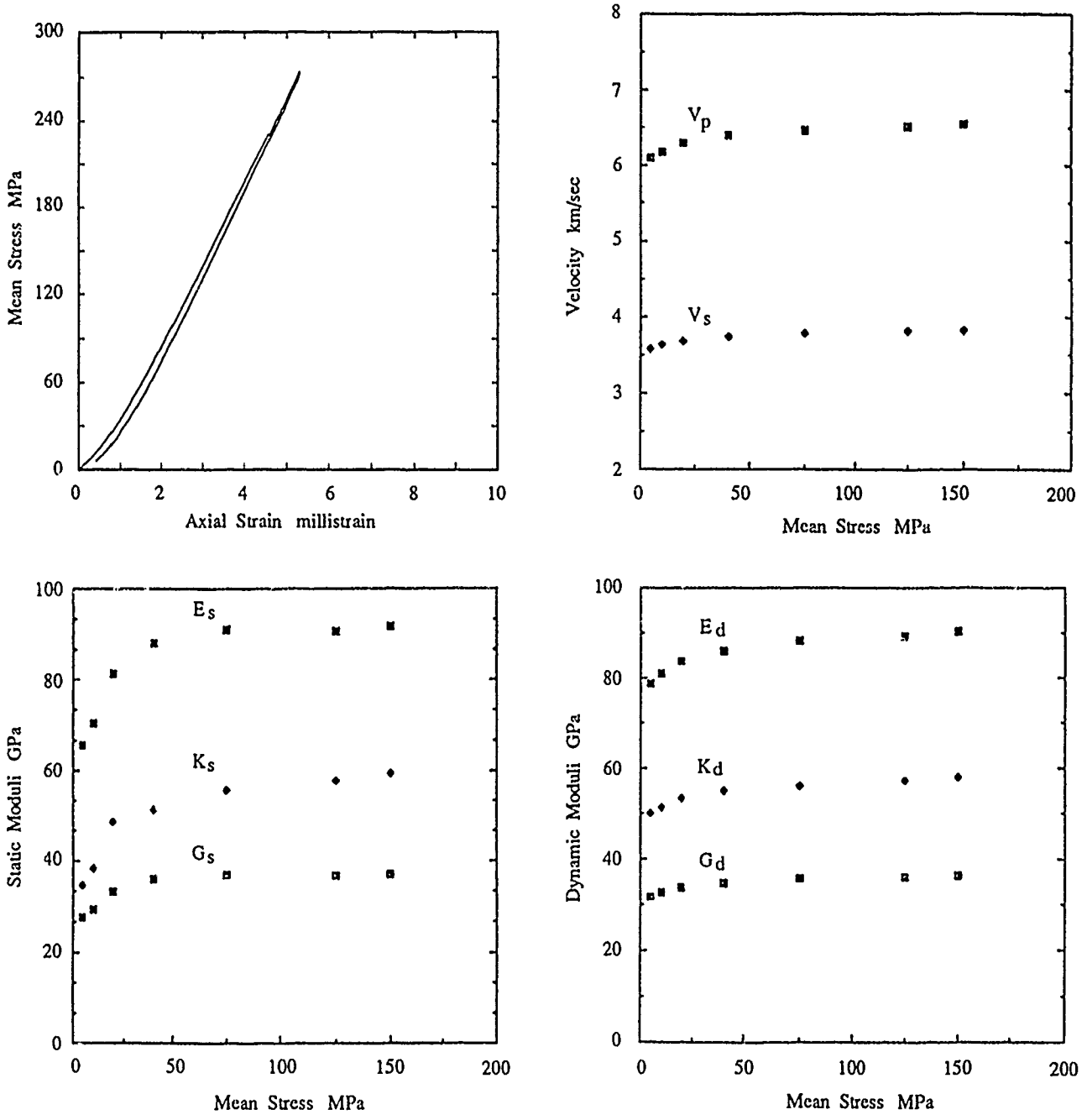

Figure B-6 Uniaxial strain experimental data for Westerly Granite sample obtained from surface outcrop from Westerly, Rhode Island.

SIERRA WHITE GRANITE

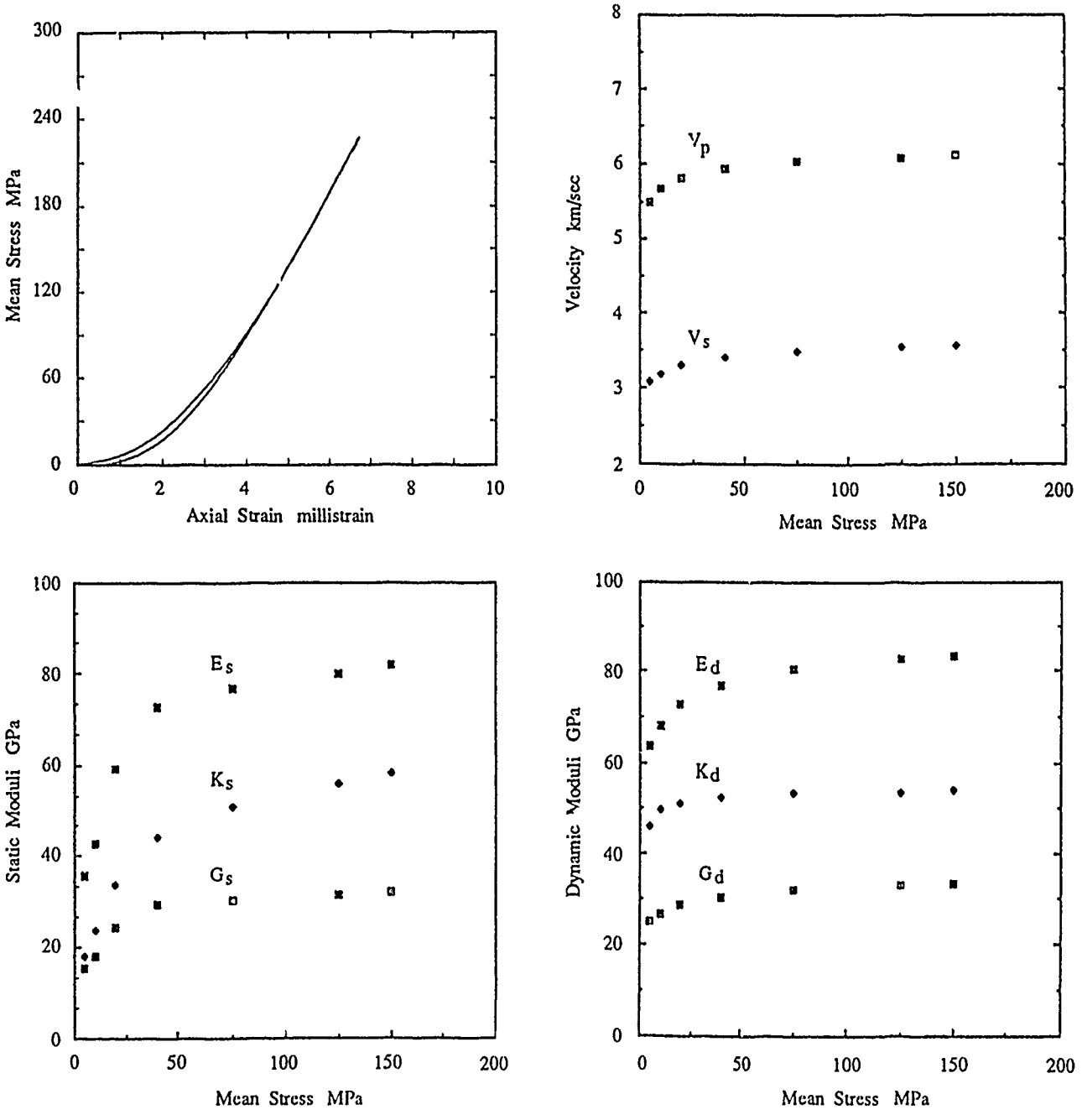

Figure B-7 Uniaxial strain experimental data for Sierra White Granite sample obtained from surface outcrop from Raymond, California.

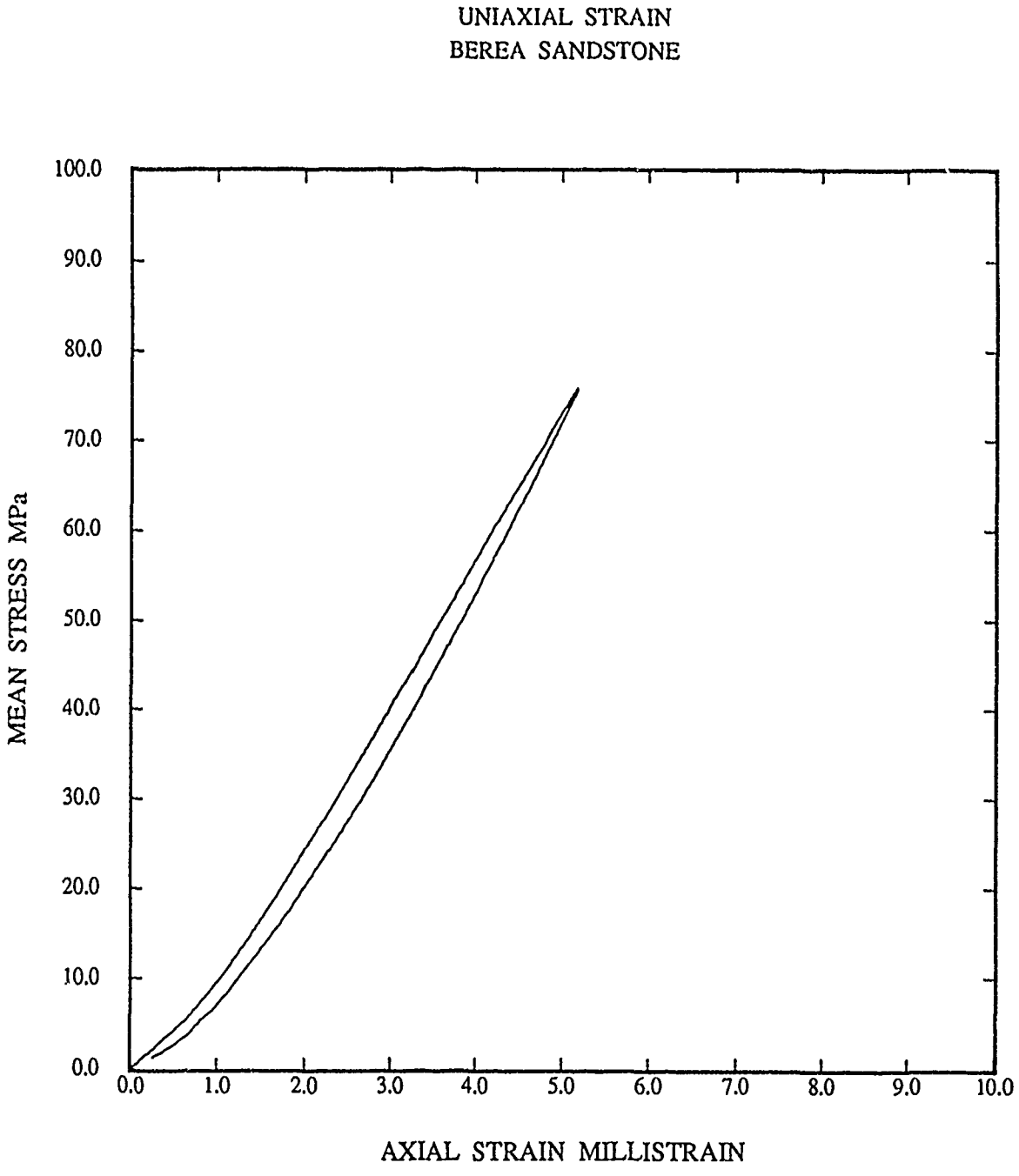
UNIAXIAL STRAIN
BEREA SANDSTONE
MEAN STRESS MPa
100.0
90.0
80.0
70.0
60.0
50.0
40.0
30.0
20.0
10.0
0.0
0.0
1.0
2.0
3.0
4.0
5.0
6.0
7.0
8.0
9.0
10.0
AXIAL STRAIN MILLISTRAIN

Figure B-8

APPENDIX C

THIN SECTION PHOTOMICROGRAPHS

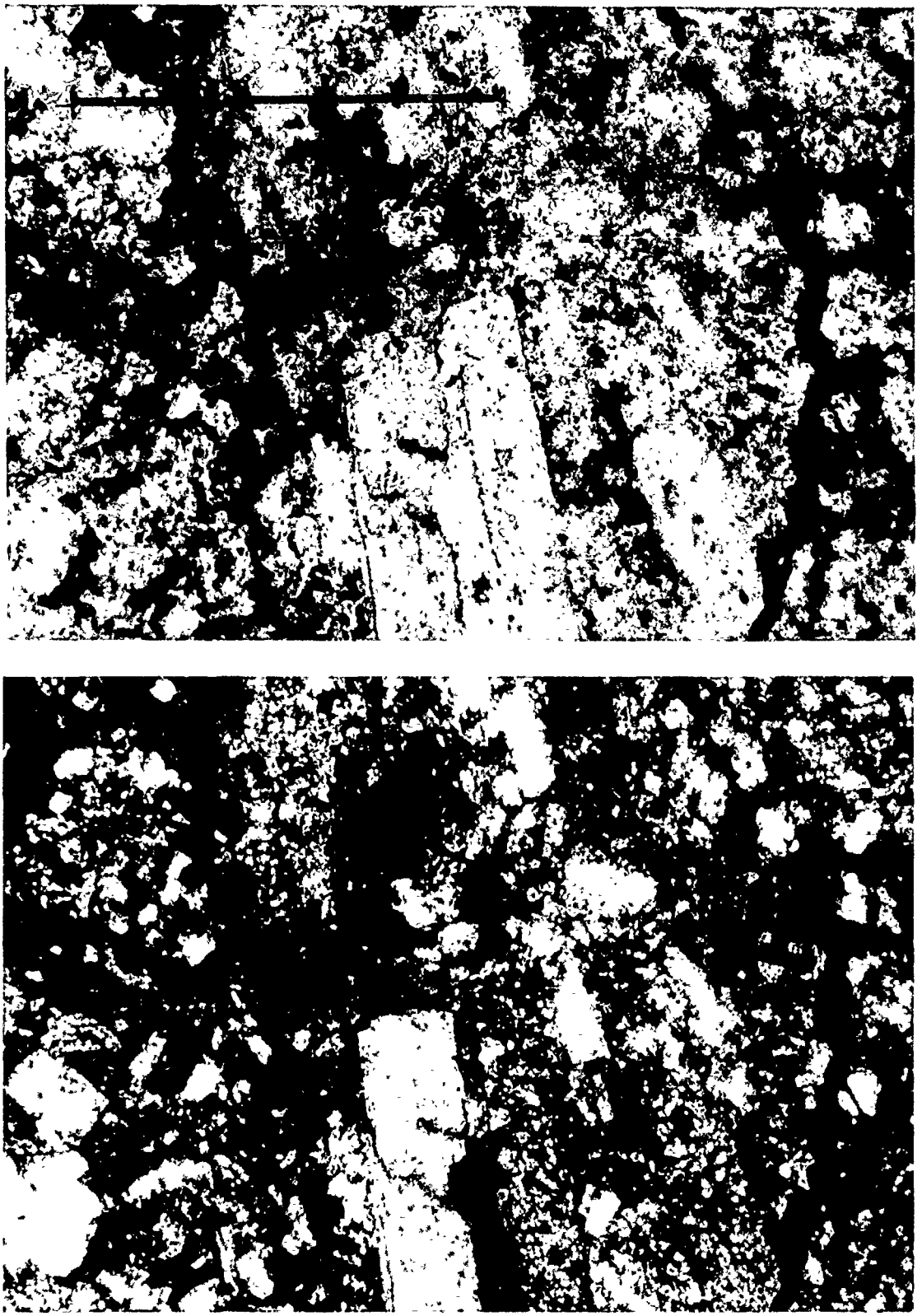

Plate C-1. Thin section photomicrographs for **Soviet sample (Altered Quartz Diorite).** The top and bottom panels are photographed with plane polarized and cross-polarized light, respectively. The scale bar measures to one millimeter and refers to both panels.

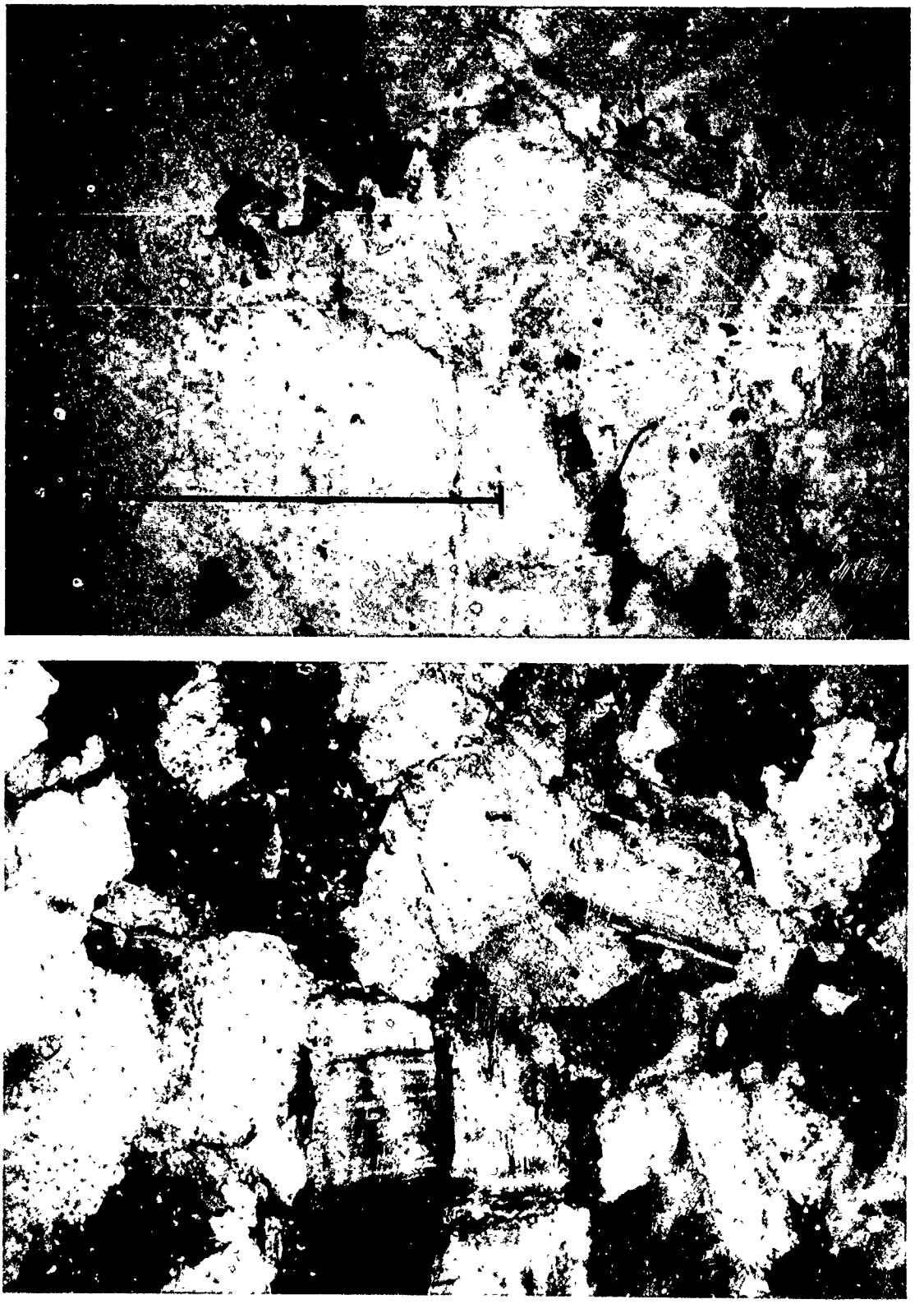

Plate C-2. Thin section photomicrographs for Soviet sample (Monzonite). The top and bottom panels are photographed with plane polarized and cross-polarized light, respectively. The scale bar measures to one millimeter and refers to both panels.

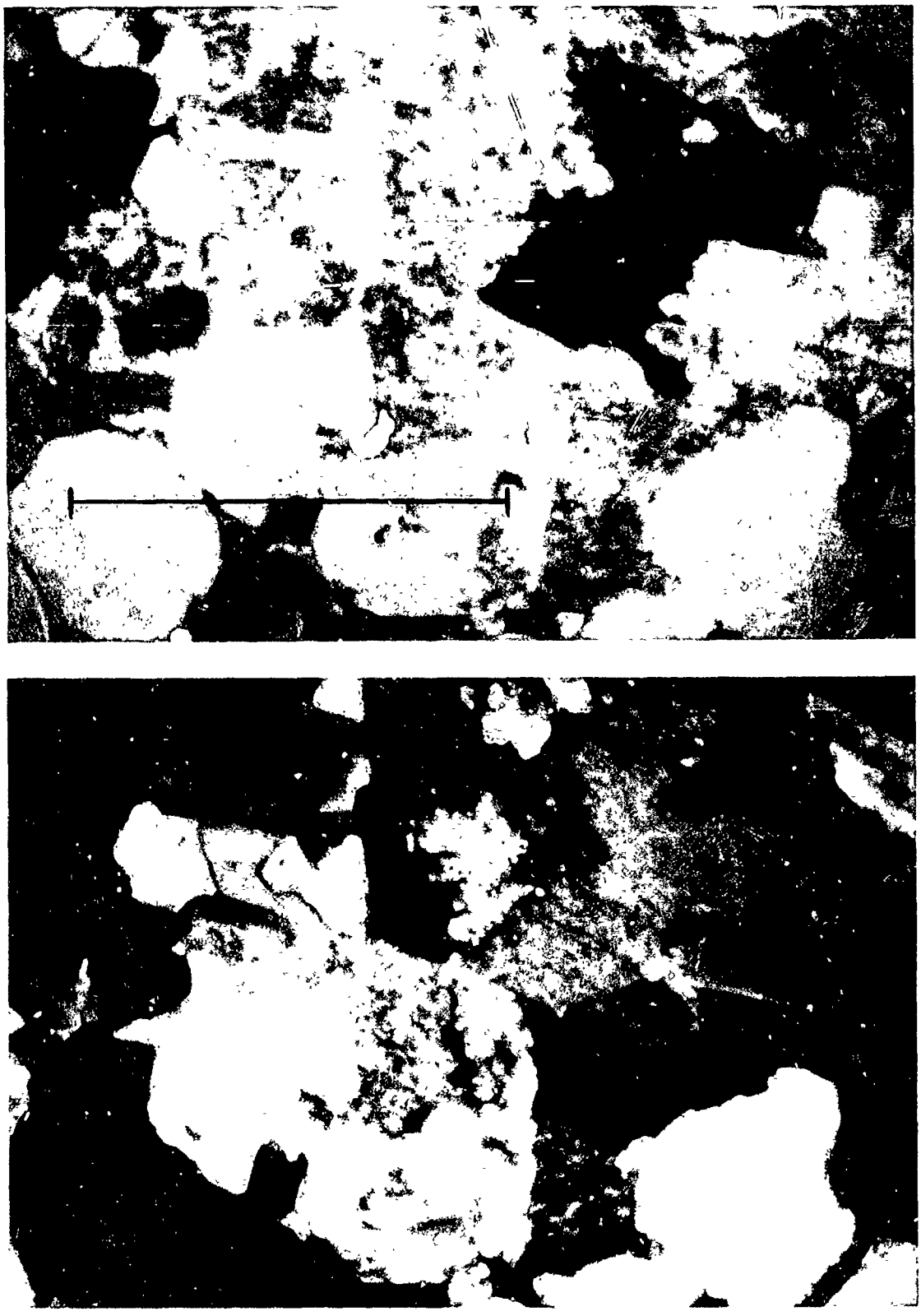

Plate C-3. Thin section photomicrographs for **Soviet sample (Granite).** The top and bottom panels are photographed with plane polarized and cross-polarized light, respectively. The scale bar measures to one millimeter and refers to both panels.

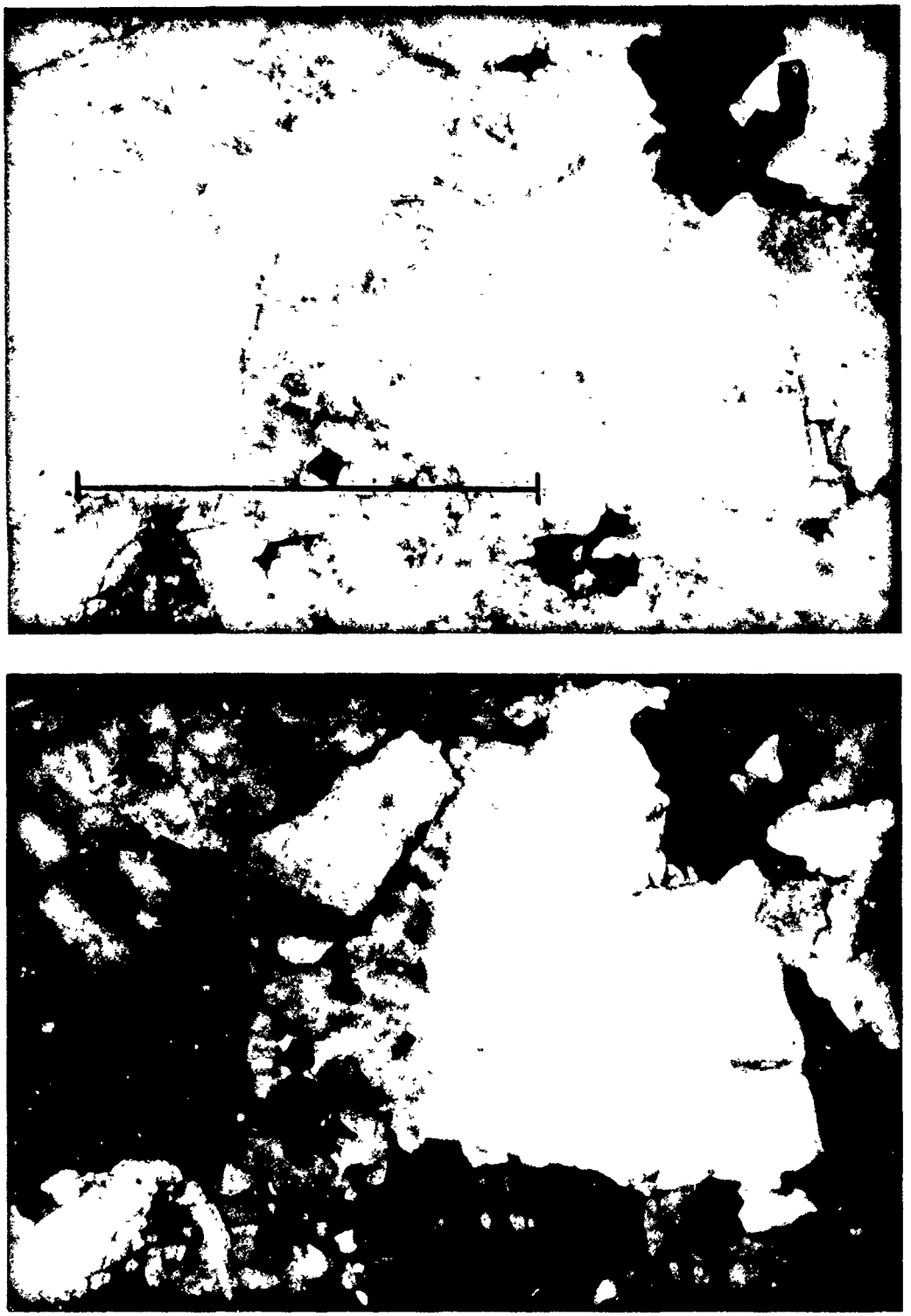

Plate C-4. Thin section photomicrographs for **Katahdin Granite (Coarse Grained).** The top and bottom panels are photographed with plane polarized and cross-polarized light, respectively. The scale bar measures to one millimeter and refers to both panels.

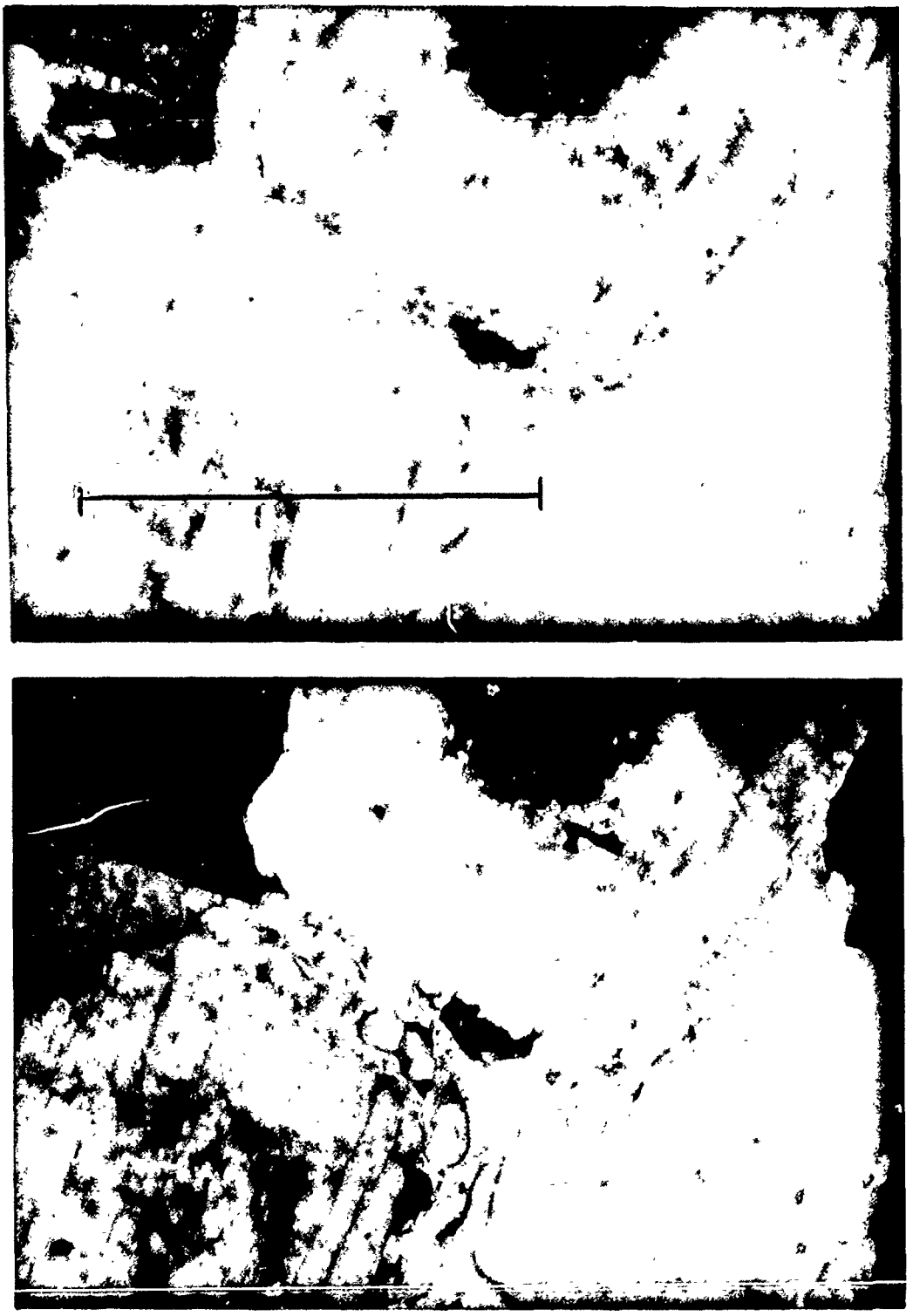

Plate C-5. Thin section photomicrographs for **Katahdin Granite (Fine Grained).** The top and bottom panels are photographed with plane polarized and cross-polarized light, respectively. The scale bar measures to one millimeter and refers to both panels.

Plate C-6. Thin section photomicrographs for **Westerly Granite.** The top and bottom panels are photographed with plane polarized and cross-polarized light, respectively. The scale bar measures to one millimeter and refers to both panels.

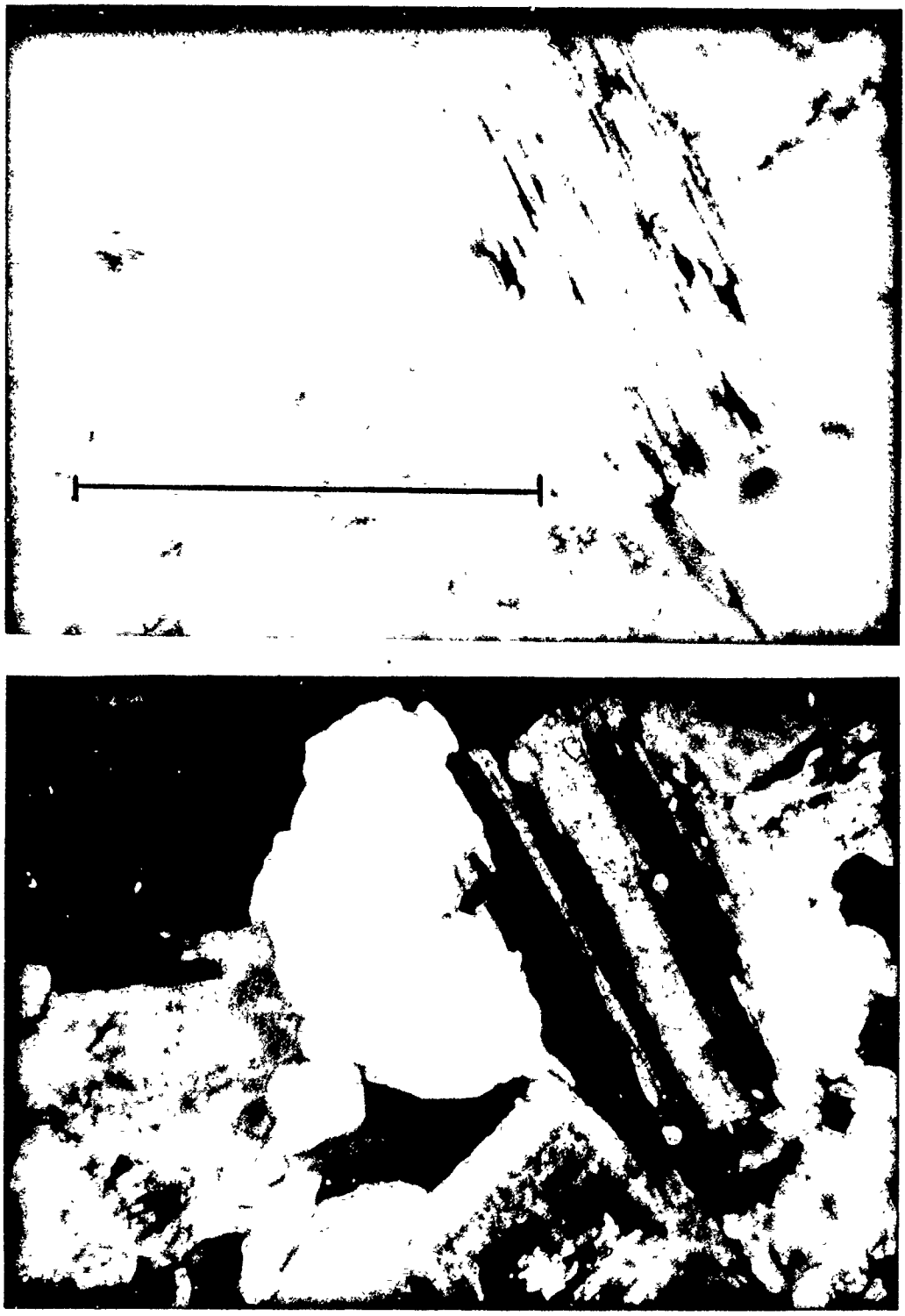

Plate C-7. Thin section photomicrographs for **Sierra White Granite.** The top and bottom panels are photographed with plane polarized and cross-polarized light, respectively. The scale bar measures to one millimeter and refers to both panels.

SECTION 2

The Strain Amplitude Dependence of Attenuation and Moduli in Sierra White Granite from Hysteresis Loops at 0.1 Hz

Karl B. Coyner
New England Research, Inc..
White River Junction, Vermont 05001

INTRODUCTION

Experimental stress-strain measurements on rocks are necessary for the understanding and interpretation of seismic nonlinearity and attenuation in the large strain-amplitude seismic nearfield. Appeals to nonlinearity and wide range of seismic Q factors are necessary in order to model the nearfield displacements and velocities of seismic wavefields in granite, tuff, and salt lithologies (Minster and Day, 1986; McCartor and Wortman, 1988). Such appeals can be investigated, or at least bounded, by direct measurements on appropriate samples.

It is well established that the transition from linear to nonlinear attenuation occurs at a strain amplitude of approximately 10^{-6} strain for a variety of rock types including limestone, granite, quartzite, anorthosite, pyroxenite, salt, and sandstone (Peselnick and Outerbridge, 1961; Gordon and Davis, 1968; Gordon and Rader, 1971; Winkler et al., 1979; Bulau and Tittmann, 1985). For saturated samples the transition may occur at a slightly lower strain amplitude than for dry samples (Winkler et al.,1979). The exact physical mechanisms are not fully understood but friction is suggested by the transition and linear relationship observed between attenuation and strain at strain amplitudes above 10^{-6}. Several theoretical models have been developed (Walsh, 1966; Mavko, 1979; Stewart et al., 1983). These models have been used to extrapolate attenuation data to very large strain amplitudes (Minster and Day, 1986) although experimental data at these amplitudes is lacking.

The resonant bar technique has been extensively used for determining strain amplitude dependence (Gordon and Davis, 1968; Winkler et al., 1979; Bulau and Tittmann, 1985). Ultrasonic experiments have also been conducted (Stewart et al., 1983; Coyner, 1987). Although the resonant bar technique is very sensitive at low attenuations and able to accurately measure the transition to nonlinear attenuation, a difficulty inherent in both of

these techniques is accessing strain amplitudes above approximately 10^{-5}. Resonant bar peaks become distorted at large strain amplitudes (Bulau and Tittmann, 1985), and accurate attenuations are difficult to determine. The strain amplitudes of ultrasonic waves in solids are difficult to measure directly and are typically estimated from linear piezoelectric relationships that are in reality only appropriate for low DC voltages.

Alternatively, the hysteresis loop technique may be used to investigate the strain amplitude and stress dependence of attenuation in the frequency range from approximately 0.01 to 100 Hz over the strain amplitude range from 10^{-9} to 10^{-2}. In this technique the stress-strain response of rock can be directly measured on samples subjected to cyclic stress which may be either a uniaxial or hydrostatic compression, torsional or flexural shear, or some combination thereof. Attenuation is computed either from the phase angle between stress and strain or else from the fractional energy loss per cycle recorded in the hysteresis loop. Previous experimental studies with this technique include Gordon and Davis (1968), Walsh et al. (1970), McKavanagh and Stacey (1974), Spencer (1981), Brennan (1981), and Liu and Peselnick (1983). Although seismic frequencies and large strain amplitudes are attained, far-field strain amplitudes less than 10^{-6} are experimentally difficult.

The experimental results described in this report are for room dry and water saturated samples of Sierra White granite. Hysteresis loops were recorded during sinusoidal, 0.1 Hz uniaxial loadings at strain amplitudes between 10^{-3} and 10^{-7}. The measurements were made in uniaxial stress, with a free boundary in the radial direction, as distinguished from uniaxial strain. The data reveal the complete transition from linear to nonlinear attenuation, the dramatic increase in attenuation due to friction on cracks, and the limitation of crack closure as an upper bound on maximum attenuation at high strain amplitudes.

EXPERIMENTAL PROCEDURE

Hysteresis loop attenuation measurements were made on a precisely ground cylinder of Sierra White granite 0.15 meters in diameter and 0.51 meter long. The sample was instrumented with three axial LVDT displacement transducers mounted on two circumferential rings positioned with radial screws approximately 3 cm from each end of the sample (Figure 1). The LVDT barrels were axially mounted in one ring while the LVDT cores were attached to the second ring with extension rods. With this arrangement sample displacement was measured between the centers of the two circumferential rings. The instrumented sample was located in series with a precision load cell in a servo-controlled loading frame. The sample was exposed to the atmosphere at room temperature. The sample column was pre-loaded to a constant axial stress of 0.1 MPa for the first series of measurements. A sinusoidal, 0.1 Hz, axial force was applied to one sample end with the servo-controlled axial ram operating in a force-feedback mode. A PC-based D/A converter was used to generate the 0.1 Hz controlling signal. A voltage divider on the D/A output controlled the amplitude of the force and thereby the strain amplitude of the hysteresis loop. Axial force from the load cell and sample displacement from the LVDT transducers were measured and recorded with a PC-based A/D converter as a function of load and strain amplitude between approximately 10^{-7} and 10^{-3} strain by varying the voltage of the sinusoidal signal driving the axial ram. The stress cycle minima were near the pre-loaded axial stress of 0.1 MPa.

The axial load and displacement data were converted to axial stress and axial strain data by simple division with sample cross-sectional area and the ring separation distance, respectively. The phase angles between stress and the three individual LVDT signals were first analyzed separately, then averaged if all three signals agreed to within 10%. This initial analysis was made immediately after each data set was acquired. If the three signals did not agree, realignment of the relative positions of axial ram, load cell, and sample usually brought the individual phase angles into agreement. When in agreement, the three individual LVDT signals were averaged and a single extensional attenuation (Q_e^{-1}) and Young's modulus (E) were computed.

Attenuation was calculated from either the phase angle between stress and strain or the area of the hysteresis loops. At low strain amplitudes the hysteresis loop area was negligible, and Q_e^{-1} was calculated from the tangent of the phase angle ϕ between axial stress and strain determined by FFT analysis ($Q_e^{-1} = \tan \phi$). At large strain amplitudes, the Q_e^{-1} was calculated from the fractional energy per cycle loss as indicated by the plotted hysteresis loops. The attenuation is defined as:

$$Q_e^{-1} = \frac{\Delta w}{2\pi W} \qquad (1)$$

where Δw is the dissipated strain energy during one cycle, or the area enclosed within the plotted hysteresis loop, and W is the maximum strain energy introduced into the sample during one stress-strain cycle, or the integrated area beneath the loading section of the cycle. Young's modulus was calculated from the least-squares fit of a straight line through the hysteresis loop.

A first set of hysteresis loop experiments were conducted on the Sierra White granite sample at a pre-load of 0.1 MPa. Additional sets of experiments were made at higher initial axial stresses of 10 MPa and 20 MPa. These data were collected in order to measure the effect of stress on attenuation. Although hydrostatic confining pressures would have been preferable for this purpose, further experimental refinements will be necessary. The higher axial stress closes microcracks normal to the stress direction, reducing attenuation and affecting the strain amplitude dependence. Similar sets of measurements were made for both the dry and saturated samples. At the larger initial loads a larger capacity load cell was necessary. This resulted, however, in less stress sensitivity and an inability to resolve low ($<10^{-6}$) strain amplitudes.

The errors in the load and strain measurements were on the order of 1% or less. The integration of hysteresis loops is accurate to within 0.5%. The phase angle calculation incurred a relatively larger error , and the corresponding Q^{-1}'s are precise to +/-15%.

EXPERIMENTAL RESULTS

A selected sequence of four hysteresis loops for Sierra White granite from low to high strain amplitudes is shown in Figures 2a and 2b. These data were collected with an initial preload of 0.1 MPa, so that one end of each hysteresis loop is essentially "pinned" at nearly zero stress and strain. In Figures 2a and 2b, the strain amplitudes decrease from left to right, top to bottom, and correspond to strain amplitudes of 491, 192, 53.5, and 27.2 microstrain. The vertical axis is stress in MPa as calculated from the recorded load cell force divided by sample cross-sectional area (29 cm^2). The horizontal axis is axial strain in units of 10^{-6} strain, or microstrain, as calculated from displacement measured by the averaged LVDT signals divided by separation distance between the rings. The energy loss is expressed by strain lagging the driving stress, so in these plots the hysteresis loop is traced out in a clockwise direction. For example, as stress reaches a maximum level and then decreases, as for the upper right hand point of any of the hysteresis loops in Figures 2a and 2b, the strain lags behind stress and falls to the right of the data along the increasing load portion of the loop.

The increase in attenuation with strain amplitude is clearly apparent in the sizes and shapes of the hysteresis loops. At low strain amplitudes, typified by the 27.2 microstrain loop in Figures 2a and 2b, the hysteresis loop is barely discernable, so that very little energy is absorbed by the sample and attenuation is quite low. With increasing strain amplitude, the size of the loop relative to the area under the loop increases, indicating increasing attenuation. Nonlinearity is indicated by the nonelliptical loop shapes and the cusped ends. The intermediate strain amplitudes of 53.5 and 192 microstrain in Figures 2a and 2b clearly show the increasing size of the hysteresis loop. Finally, at the largest strain amplitude for which data were recorded, 491 microstrain, the hysteresis loop is both large as well as asymmetrical. The loop at lower stresses and strains is lobately shaped while at the higher stresses and strains it is narrower and more pointed. This shape is due to the behavior of microcracks during the hysteresis loop cycle. At low stresses there is a large population of low aspect ratio microcracks that are opening and closing and sliding across one another. Frictional sliding and attenuation at low stresses is maximized because of the substantial population of microcracks, giving rise to the asymmetry of the hysteresis loop.

The hysteresis loop data collected with a 10 MPa uniaxial stress are shown in Figures 3a, 3b, 3c and 3d. This set of loops is distinct from the previous set shown in Figures 2a and 2b in that the centers of all the loops are coincident at 10 MPa uniaxial stress, with the cyclic driving stress ranging symmetrically to either side of this initial stress. The loops are split into two subsets. A collection of four low strain amplitude loops are shown in Figures 3a and 3b and a second subset of four high strain amplitude loops are shown in Figures 3c and 3d. Although the two scales in the four figures are different, the aspect ratio of stress versus strain is the same, so that the slopes of the loop data are comparable.

As before, the effects of strain amplitude on attenuation are revealed in the relative sizes and shapes of the hysteresis loops. The hysteresis loops are small, nearly straight lines at the low strain amplitudes in Figures 3a and 3b. At the intermediate strain amplitudes in Figures 3a, 3b, 3c and 3d, well-defined loops occur as attenuation increases. At the largest strain amplitudes in Figure 3d, the loops become asymmetrical and quite large because the low stresses open and close the most compliant microcrack population. Zero stress is the limiting factor to strain amplitude in these experiments because the uniaxial stress cannot become negative, or cause the sample to go into tension, with the experimental setup. Because the centers of the hysteresis loops in Figures 3a, 3b, 3c and 3d are coincident, the attenuations and moduli are appropriately comparable. In addition to variation in attenuation, the slopes can be used to calculate Young's modulus as a function of strain amplitude. The hysteresis loop Young's modulus, or the tangent to the hysteresis loop at 10 MPa stress, decreases as strain amplitude increases in Figures 3a, 3b, 3c and 3d. This phenomenon is closely related to the static versus dynamic modulus problem and is discussed in the following section.

DISCUSSION

The hysteresis loop extensional attenuations for dry Sierra White granite are plotted versus the log of strain amplitude in Figure 4. The three curves correspond to uniaxial stresses of 0.1, 10, and 20 MPa. The transition from linear to nonlinear attenuation at a strain amplitude of approximately $5*10^{-6}$ is most pronounced in the data collected at a uniaxial stress of 0.1 MPa. A similar threshold at approximately $3*10^{-5}$ is also noted for the data collected at a uniaxial stress of 20 MPa. This difference is consistent with a frictional attenuation mechanism that gives rise to the threshold. At the higher uniaxial stress a large proportion of the microcrack surfaces and point contacts are locked together. Hence, it requires a larger strain amplitude in order to activate frictional attenuation and nonlinearity.

Three distinct regions of behavior are exhibited by the curves in Figure 4. The first region is below the threshold: attenuation is linear and constant with strain amplitude. The exact level of attenuation is closely related to the moisture content of rock (Tittmann, 1977). The second region is above the threshold and reveals a rapidly increasing attenuation with increasing strain amplitude. In this region the frictional attenuation mechanism dominates. Friction is not unlimited, however, and this gives rise to the third region of behavior at strain amplitudes above approximately $2*10^{-4}$. At these amplitudes the crack surfaces and point contacts across which friction has been occurring slide to the maximum extent possible and essentially become closed or locked together at the large stresses and strains. Maximum attenuation is achieved and the strain amplitude dependence levels off. In Figure 4 it is also apparent that attenuation may actually decrease. This is explained on the

basi: .f the the attenuation definition. Although the size of the hysteresis loop may not increase because friction has maximized, the area under the hysteresis loop, or the energy introduced into the sample, continues to increase. Therefore, the calculated attenuations tend to decrease as strain amplitudes increase.

The effect of water saturation on the strain amplitude dependence of extensional attenuation is shown in Figure 5, hich is a plot similar to Figure 4 with the three different uniaxial stresses. Extensional attenuation nearly doubles in the water-saturated sample because of fluid flow attenuation mechanisms. The strain amplitude dependence still shows three regions of behavior similar to those for the dry sample, however. The threshold amplitude for nonlinearity may occur at a lower strain than in the corresponding dry case.

Linear Dependence on Strain Amplitude

Both simple concepts of friction and detailed models require that attenuation be linearly dependent on strain amplitude (Walsh, 1966; Mavko, 1979; Stewart et al., 1983). In Figure 6 the hysteresis loop attenuations at 0.1 MPa axial load are plotted as a function of strain amplitude on a linear scale. At amplitudes less than approximately 50 microstrain the relationship does indeed appear to be linear as indicated by the dashed line. The effects of crack closure are seen at higher strains, and the attenuation falls below the extrapolated linear relationship. At these strains the cracks which give rise to attenuation are closing and can contribute little more at higher strain amplitudes. This crack closure was directly observed by Batzle et al. (1980) at similar stresses and strains for granite. The crack closure limit will depend on crack density, hence lithology, and, in the field, on the presence of larger scale joints and fractures. Similar experiments on fractured specimens and other model studies will be reported on in the future.

The decrease in attenuation above 200 microstrain in Figures 4 and 6 is a result of the attenuation definition of fractional energy loss. Any small increase in energy loss is offset by the larger increase in energy stored during one cycle of the sinusoidal loading, and the attenuation calculated from the ratio actually decreases. This decrease presumably continues with increasing strain amplitude until a large population of new cracks form in conjunction with brittle failure. For Sierra White granite this occurs at around 5000 microstrain.

Static versus Dynamic Moduli

Strain amplitude also has a sizable effect on modulus that is concurrent with its effect on attenuation. The hysteresis loop experiments in this study measured variations in nonlinear attenuation through the relative sizes of the hysteresis loops. The slope of the

major axis of each hysteresis loop, meanwhile, is Young's modulus, and these slopes are also rotating with strain amplitude such that Young's modulus decreases with increasing strain amplitude. The strain amplitude dependence of Young's modulus is another aspect of nonlineartity in rock due to microcracks. It is reasonable to expect that microcracks cause a similar strain amplitude dependence for the shear and bulk moduli.

The strain amplitude dependence of bulk modulus in rock has been previously cast as a phenomenon of contrasting "static" to "dynamic" modulus, implying a frequency dependence. Simmons and Brace (1965) and Cheng and Johnston (1981) experimentally investigated the dynamic bulk modulus determined from ultrasonic P- and S-wave velocity measurements and the static bulk modulus determined from hydrostatic compression data. Both noted larger dynamic modulus versus the static, and that the maximum difference measured at low pressures decreases as pressure increases, tending to converge at pressures on the order of several kilobars. Cheng and Johnston (1981) showed with a fairly continuous data set that the difference is a function of the microcrack porosity (Walsh, 1965) of the rock at any given pressure. As confining pressure increases the static and dynamic moduli converge as the microcrack population is reduced through crack closure mechanisms. At confining pressures less than 10 MPa they observed static to dynamic bulk modulus ratios on the order of 0.4 to 0.5 for Westerly granite, Bedford limestone, and Berea and Navajo sandstones, slightly less values for a tuff, and slightly higher values for colorado oil shale. This extensive set of data for Sierra White, Westerly, and the Katahdin granites presented earlier in this report shows similar trends.

It has been previously shown (Coyner, 1990) that Young's modulus of dry Sierra White granite is nearly frequency independent as measured by hysteresis loop data at frequencies of 0.1 KHz, resonant bar data at 10 KHz, ultrasonic P and S velocity and 600-1.2 MHz bands. Therefore, frequency is not the cause of the static to dynamic modulus ratio in dry rocks.

An alternative consideration is the strain amplitudes of the individual measurements. Ultrasonic P and S wave velocities are typically measured with pulses operating at strain amplitudes of less than 10^{-6}. Quasi-static compression tests, on the other hand, are typically conducted over strain amplitudes on the order of 10^{-4} to 10^{-3}. This difference in strain amplitude gives rise to the contrast of static versus dynamic modulus. At the low strain amplitudes of ultrasonic pulses the rock sample appears stiffer than at the high strain amplitudes of uniaxial compression.

The strain amplitude effect can be clearly seen by examining the Young's modulus data determined from the hysteresis loops as a function of strain amplitude in Figures 3a, 3b, 3c and 3d. As described previously, the hysteresis loops are negative and positive excursions in stress and strain about this point. The smallest hysteresis loop is recorded at 24.6 microstrain and the largest at 659 microstrain. Although the scales change between these four figures, the aspect ratio does not. Young's modulus is the average slope drawn through the hysteresis loops. The effect of strain amplitude on the average Young's

modulus is seen in the clockwise rotation of the slope as strain amplitude increases. At lower strain amplitudes the hysteresis loop Young's modulus is larger, or the sample is responding more stiffly. As strain amplitude increases, the slope decreases so that the average material response is softer, i.e., the modulus has decreased.

The Young's modulus and strain amplitude data in Figures 3a, 3b, 3c and 3d are tabulated in Table 1. The columns list strain amplitude, Young's modulus, and $1000/Q_e$ for the Sierra White granite sample at a uniaxial load of 10 MPa. At the largest strain amplitude of 659 microstrain the Young's modulus is 30.0 GPa; at the smallest strain amplitude of 24.6 microstrain the Young's modulus is 35.3 GPa. The trend of increasing Young's modulus and decreasing extensional attenuation towards the lower strain amplitudes is evident. The ultrasonic dynamic modulus for this sample at 10 MPa uniaxial stress has not been measured at this time. Ultrasonic P and S velocities at a hydrostatic confining pressure of 10 MPa have, however, been previously measured (Coyner, 1990) and these indicate that Young's modulus is 54 GPa. This value is somewhat larger than the largest Young's modulus (35.3 GPa) measured with the hysteresis loops. There are two reasons for this. First, the ultrasonic data, collected on a sample under hydrostatic pressure, will result in a higher Young's modulus than the hysteresis loop data collected on a sample under uniaxial stress. This is because the hydrostatic pressure will close more microcracks than the uniaxial stress, which will preferentially close microcracks normal to the direction of the stress. Secondly, the lowest strain amplitude in Table 1 is still 24.6 microstrain. A rough linear extrapolation to lower strain amplitudes indicates that Young's modulus probably increases to nearly 40 GPa at less than 1 microstrain.

CONCLUSIONS

The threshold of linear to nonlinear attenuation between 10^{-6} and 10^{-5} strain is clearly evident in the hysteresis loop data at 0.1 Hz for Sierra White granite. At less than $5 * 10^{-6}$ the attenuation is independent of strain amplitude. At strain amplitudes greater than this threshold, attenuation increases rapidly. The dependence on strain amplitude is linear, in agreement with a frictional attenuation mechanism, up to approximately 50 microstrain. The increase is limited by maximum friction across crack surfaces and at point contacts. Maximum Q_c^{-1} of about 0.035 is attained at $2*10^{-4}$ strain. Young's modulus also shows a strain amplitude dependence corresponding to the nonlinearity in attenuation. The modulus decreases as a function of increasing strain amplitude. The effect of friction on modulus is a direction of further investigation.

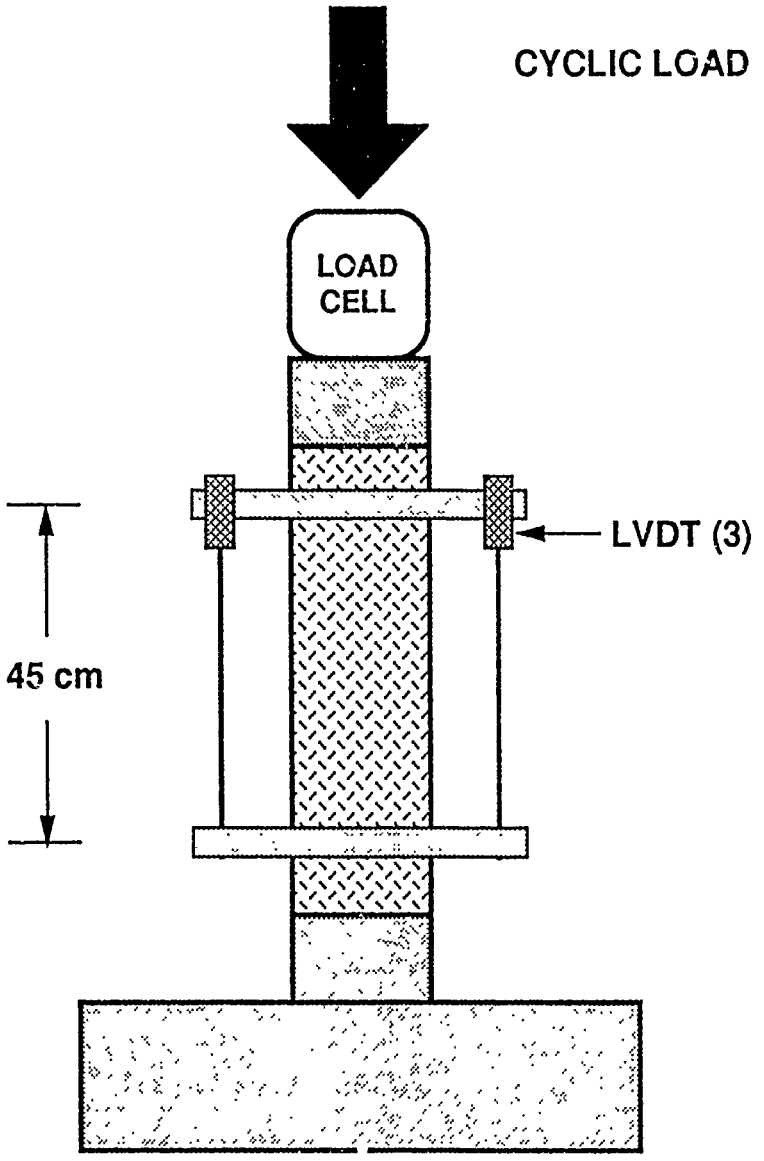

Figure 1. Schematic diagram of the experimental apparatus for low-frequency hysteresis loop modulus and attenuation measurements.

TABLE 1

Strain Amplitude, Young's modulus, and extensional attenuation from hysteresis loops at 10 MPa

Strain Amplitude (microstrain)	Young's Modulus (GPa)	Extensional Attenuation ($1000 / Q_e$)
24.6	35.3	9.7
48.5	34.9	12.6
95.4	34.0	19.0
118	33.8	22.7
221	32.7	29.5
389	31.5	31.9
573	30.5	31.8
659	30.0	31.8

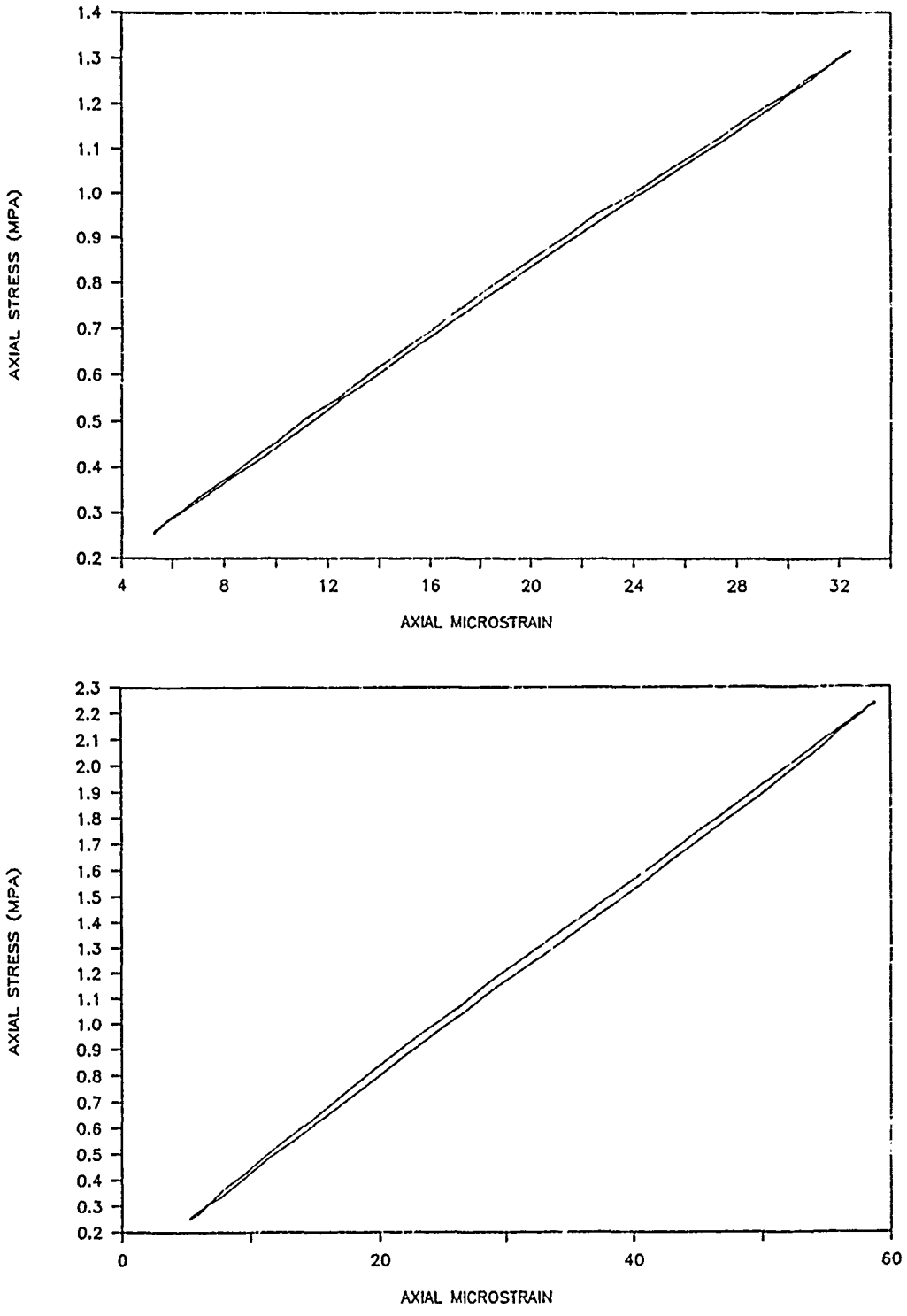

Figure 2a. A suite of hysteresis loops for Sierra White granite are plotted as a function of strain amplitude. For the ninety-degree rotated orientation, loop amplitudes increase from the top to bottom plots, corresponding to maximum strain amplitudes of 27.2 and 53.5 microstrain.

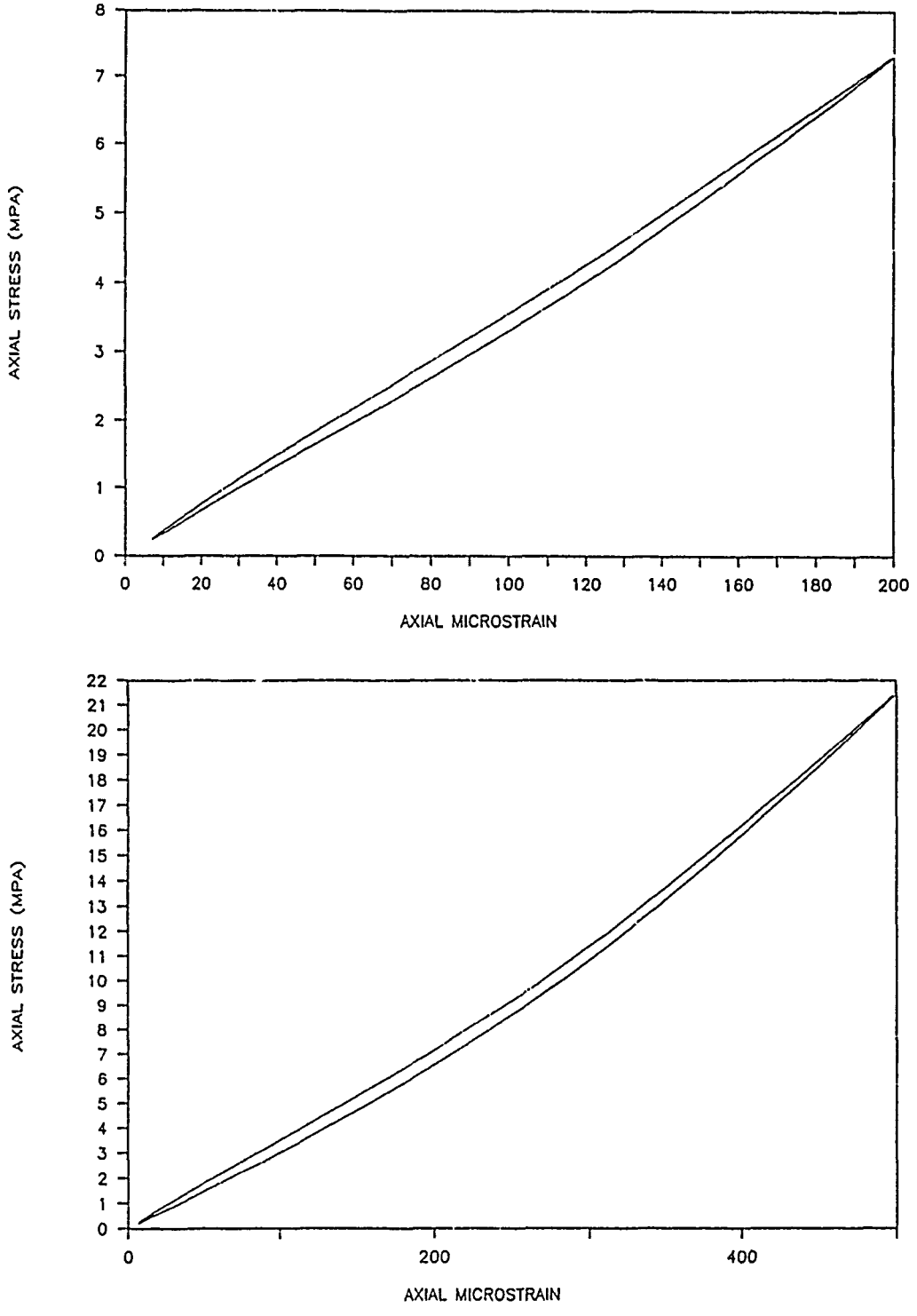

Figure 2b. A suite of hysteresis loops for Sierra White granite are plotted as a function of strain amplitude. For the ninety-degree rotated orientation, loop amplitudes increase from the top to bottom plots, corresponding to maximum strain amplitudes of 192 and 491 microstrain.

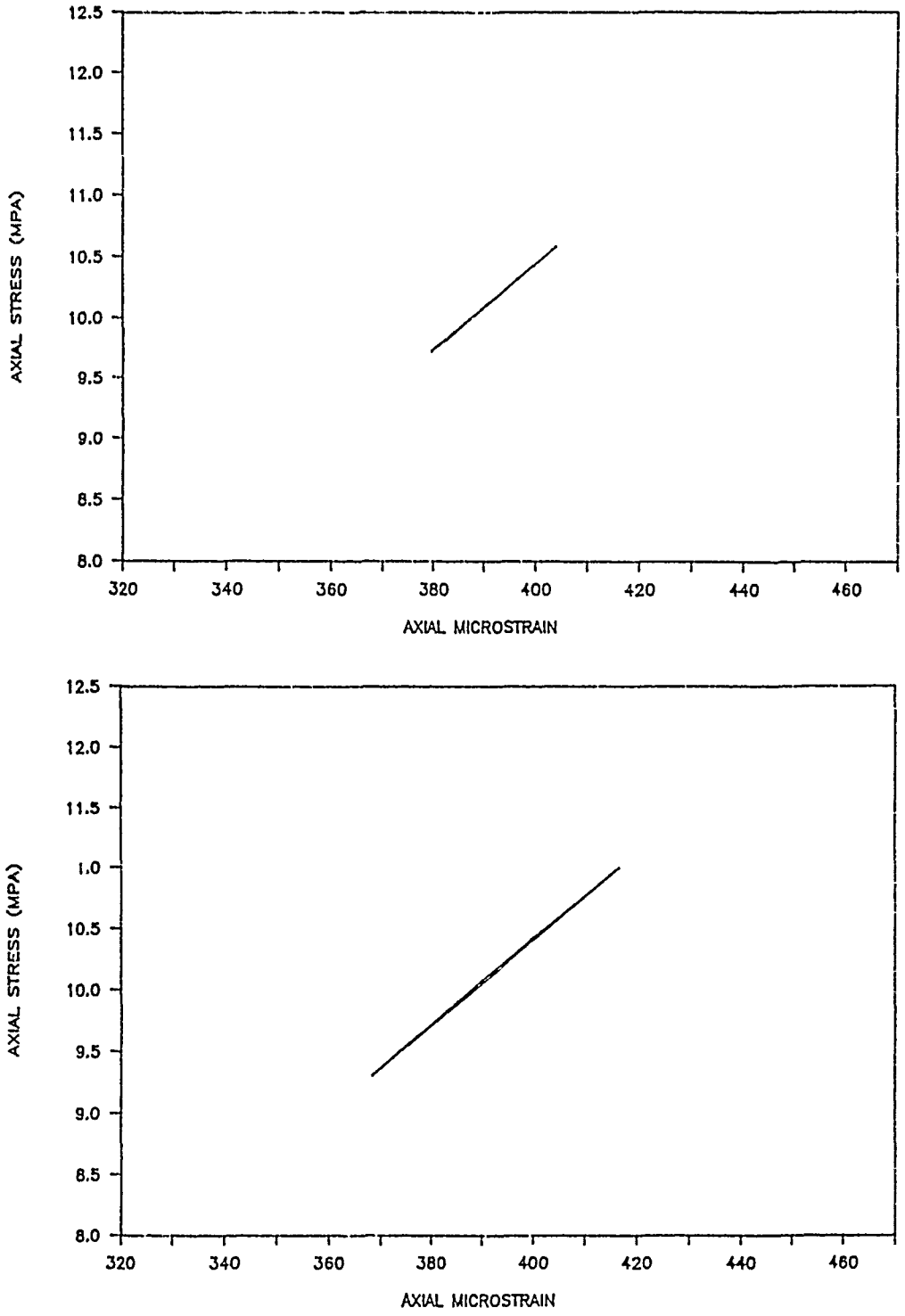

Figure 3a. Hysteresis loops for Sierra White granite sample subjected to 10 MPa uniaxial stress plotted as a function of strain amplitude.

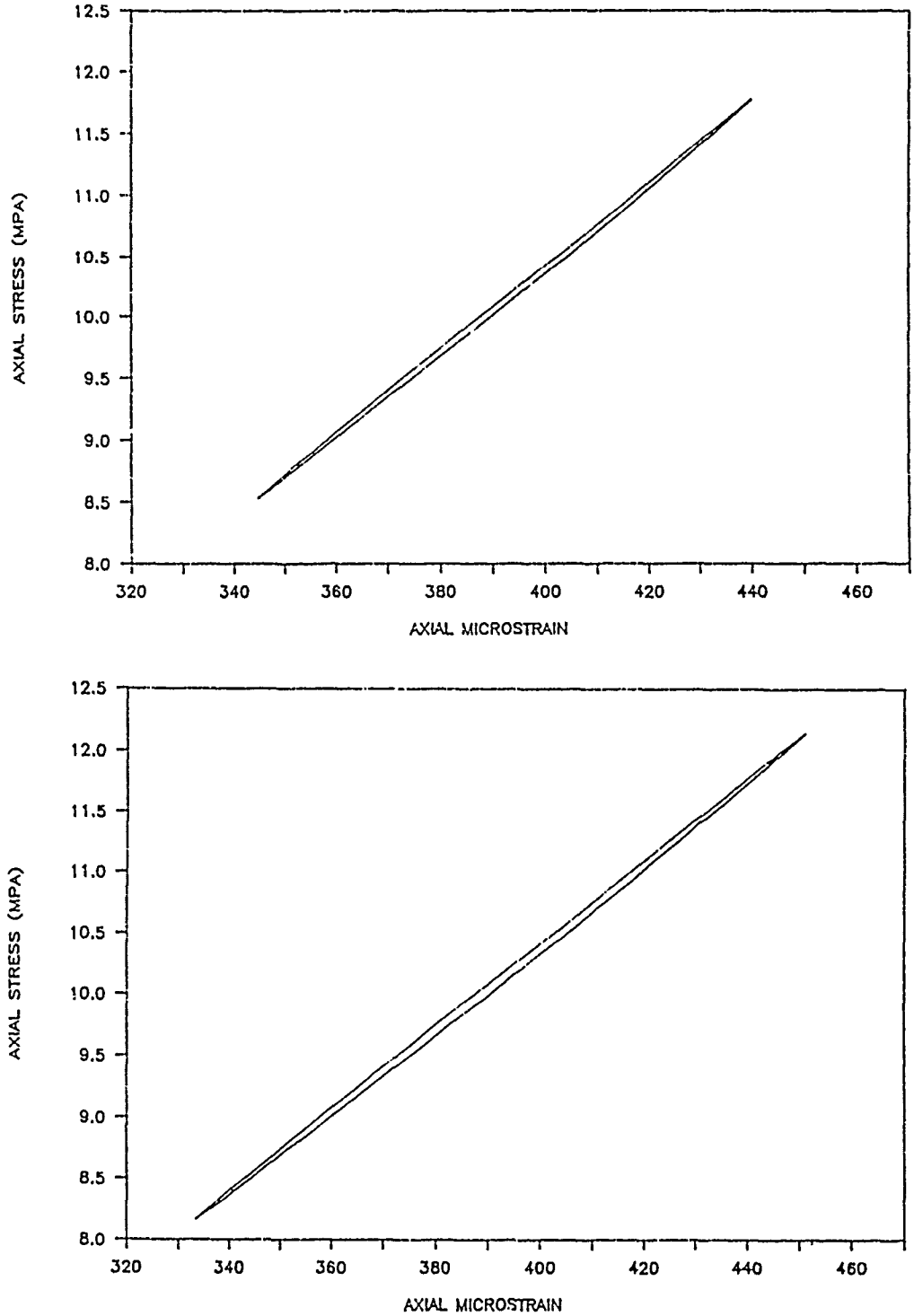

Figure 3b. Hysteresis loops for Sierra White granite sample subjected to 10 MPa uniaxial stress plotted as a function of strain amplitude.

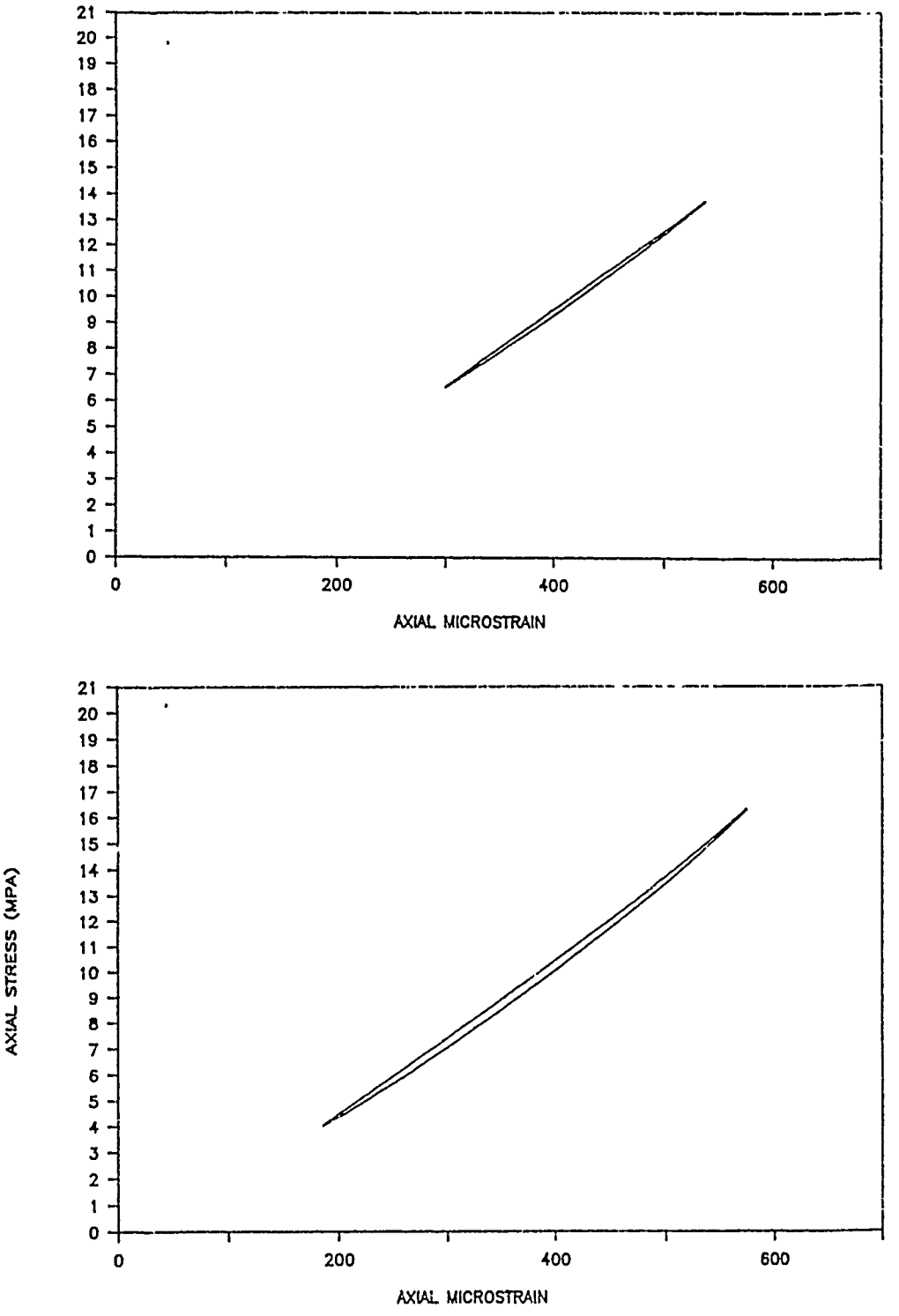

Figure 3c. Hysteresis loops for Sierra White granite sample subjected to 10 MPa uniaxial stress plotted as a function of strain amplitude.

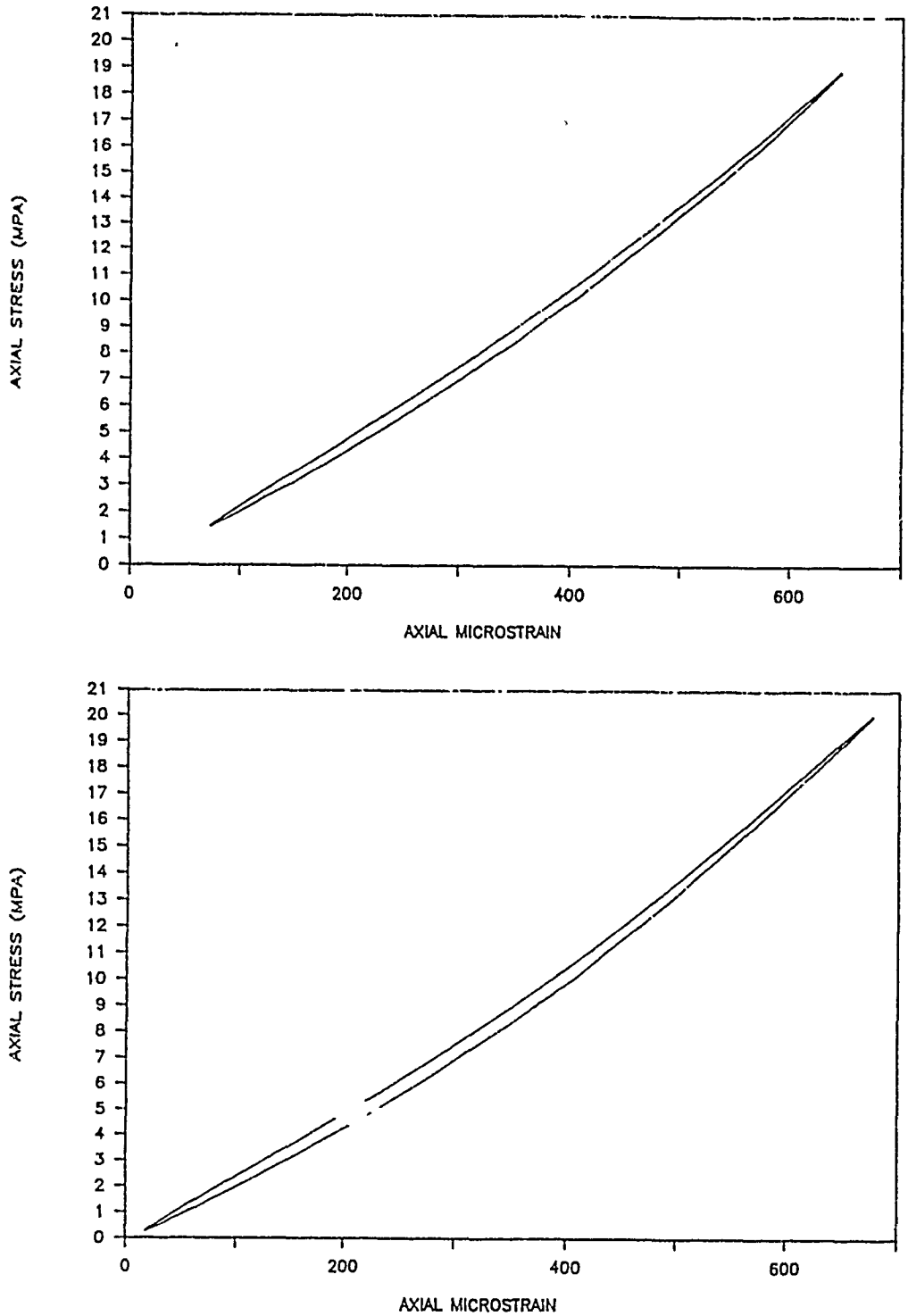

Figure 3d. Hysteretic loops for Sierra White granite sample subjected to 10 MPa uniaxial stress plotted as a function of strain amplitude.

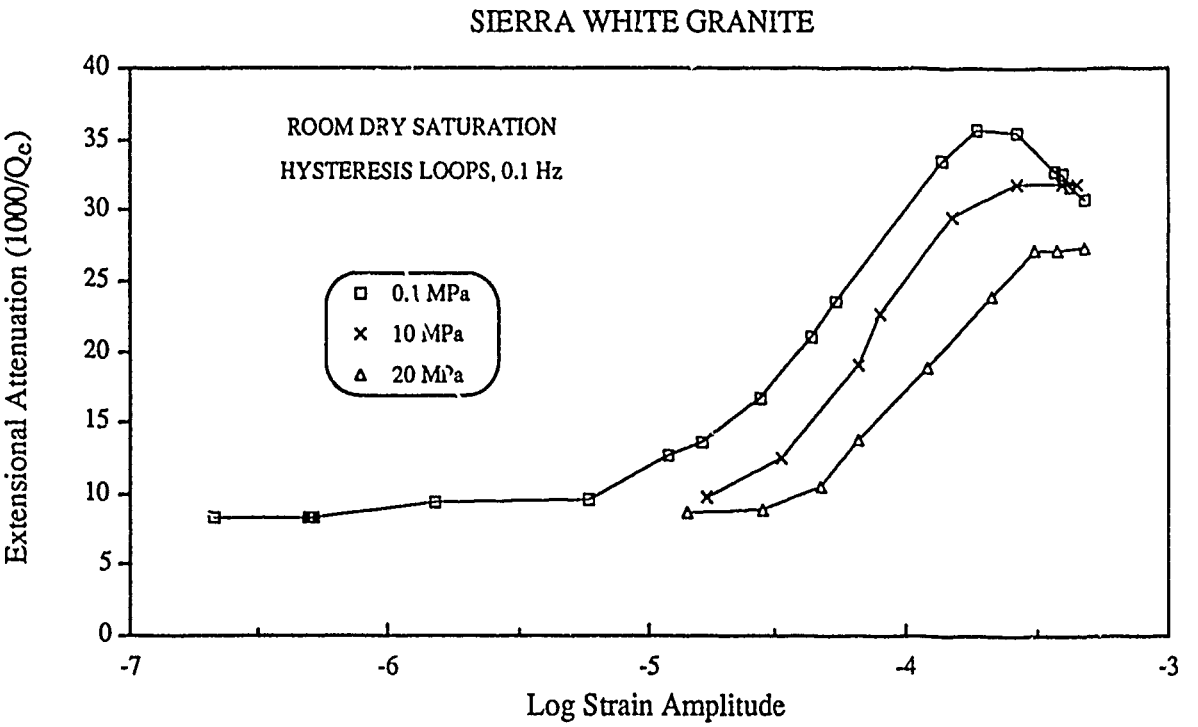

Figure 4. Strain amplitude versus extensional attenuation for dry Sierra White granite sample subjected to 0.1 MPa, 10 MPa, and 20 MPa uniaxial stress.

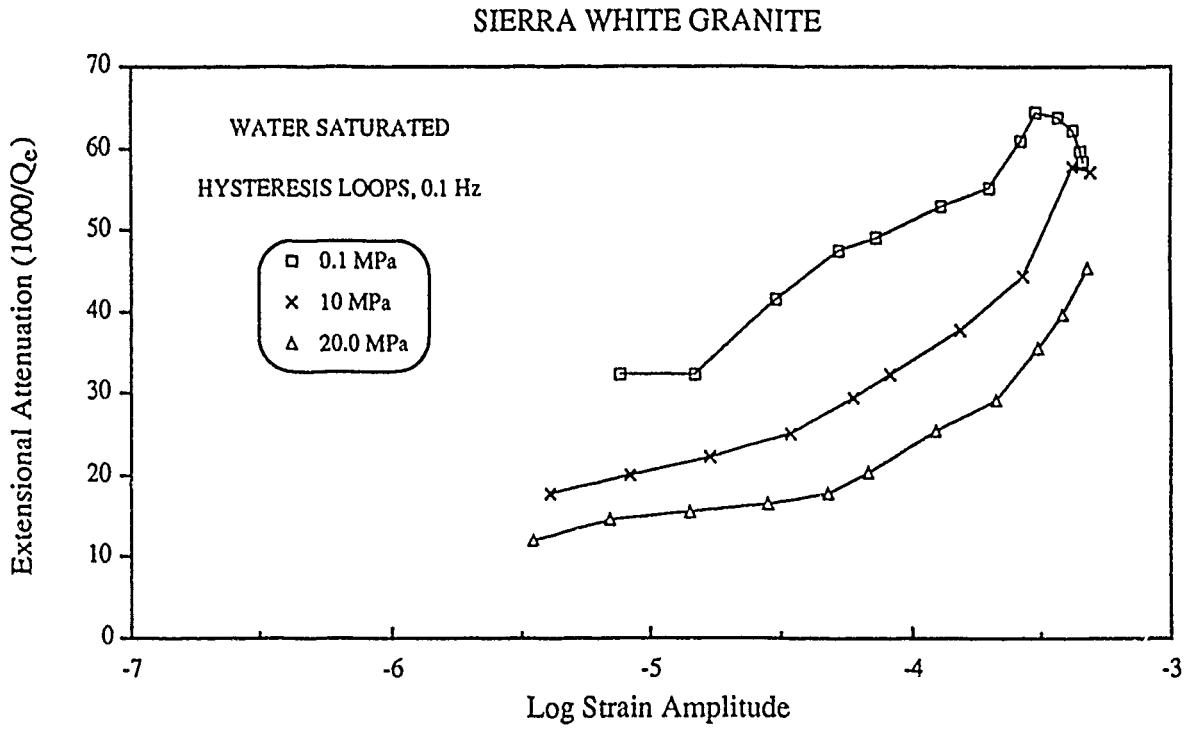

Figure 5. Strain amplitude versus extensional attenuation for water saturated Sierra White granite sample subjected to 0.1 MPa, 10 MPa, and 20 MPa uniaxial stress.